

Model BOSS & eBOSS Luminous Red Galaxies at $0.2 < z < 1.0$ using SubHalo Abundance Matching with 3 parameters

Jiayi Yu,^{1*} Cheng Zhao,^{1†} Chia-Hsun Chuang,^{2,3‡} Julian E. Bautista,⁴ Ginevra Favole,¹ Jean-Paul Kneib,^{1,5} Faizan G. Mohammad,⁶ Ashley J. Ross,⁷ Anand Raichoor,⁸ Charling Tao,⁴ Kyle Dawson,² Graziano Rossi⁹

¹Laboratory of Astrophysics, École Polytechnique Fédérale de Lausanne (EPFL), Observatoire de Sauverny, CH-1290 Versoix, Switzerland

²Department of Physics and Astronomy, University of Utah, Salt Lake City, UT 84112, USA

³Kavli Institute for Particle Astrophysics and Cosmology, Stanford University, 452 Lomita Mall, Stanford, CA 94305, USA

⁴Aix Marseille Univ, CNRS/IN2P3, CPPM, Marseille, France

⁵Aix Marseille Université, CNRS, LAM (Laboratoire d'Astrophysique de Marseille) UMR 7326, F13388, Marseille, France

⁶Waterloo Centre for Astrophysics, Dept. of Physics and Astronomy, University of Waterloo, 200 University Ave. W., Waterloo ON N2L 3G1, Canada

⁷Department of Astronomy, The Ohio State University, 140 W. 18th Ave., Columbus, OH 43210, USA

⁸Lawrence Berkeley National Laboratory, 1 Cyclotron Road, Berkeley, CA 94720, USA

⁹Department of Astronomy and Space Science, Sejong University, 209, Neungdong-ro, Gwangjin-gu, Seoul, South Korea

Accepted XXX. Received YYY; in original form ZZZ

ABSTRACT

SubHalo Abundance Matching (SHAM) is an empirical method for constructing galaxy catalogues based on high-resolution N -body simulations. We apply SHAM on the UNIT simulation to simulate SDSS BOSS/eBOSS Luminous Red Galaxies (LRGs) within a wide redshift range of $0.2 < z < 1.0$. Besides the typical SHAM scatter parameter σ , we include v_{smear} and V_{ceil} to take into account the redshift uncertainty and the galaxy incompleteness respectively. These two additional parameters are critical for reproducing the observed 2PCF multipoles on $5\text{--}25 h^{-1}$ Mpc. The redshift uncertainties obtained from the best-fitting v_{smear} agree with those measured from repeat observations for all SDSS LRGs except for the LOWZ sample. We explore several potential systematics but none of them can explain the discrepancy found in LOWZ. Our explanation is that the LOWZ galaxies might contain another type of galaxies which needs to be treated differently. The evolution of the measured σ and V_{ceil} also reveals that the incompleteness of eBOSS galaxies decreases with the redshift. This is the consequence of the magnitude lower limit applied in eBOSS LRG target selection. Our SHAM also set upper limits for the intrinsic scatter of the galaxy–halo relation given a complete galaxy sample: $\sigma_{\text{int}} < 0.31$ for LOWZ at $0.2 < z < 0.33$, $\sigma_{\text{int}} < 0.36$ for LOWZ at $0.33 < z < 0.43$, and $\sigma_{\text{int}} < 0.46$ for CMASS at $0.43 < z < 0.51$. The projected 2PCFs of our SHAM galaxies also agree with the observational ones on the 2PCF fitting range.

Key words: method: numerical – method: observational – galaxy: halo – cosmology: large-scale structure of Universe

1 INTRODUCTION

Lambda-Cold-Dark-Matter (Λ CDM) has been the standard cosmological model since the 1990s. Under this framework, observations confirm that dark matter (DM) is the dominant matter component of the Universe (e.g., Planck Collaboration et al. 2020). DM particles interact only through gravity and their gravitational evolution is assumed to start from a primordial Gaussian random field with perturbations. If the over-density arising from the perturbation on small scales is large enough, the infall of matter can overcome the expansion of Universe, and form gravitational-bound clusters, i.e.,

DM haloes. Perturbations on large scales evolve into web-like structures known as the cosmic web (Bond et al. 1996). Baryonic matter may be captured by haloes with deep potential wells and further evolve into galaxies (Press & Schechter 1974; White & Rees 1978), a good tracer of the invisible cosmic web.

Galaxy surveys explore the large-scale structure of the Universe by measuring the redshifts of millions of galaxies and quasars. Their positions can be used to calculate the two-point correlation function (2PCF) that encodes the history of the universe expansion and the structure growth. The Baryon Oscillation Spectroscopic Survey (BOSS, 2008–2014; Dawson et al. 2012) is the largest project in the third-stage Sloan Digital Spectroscopic Survey¹ (SDSS-III; Eisen-

* E-mail: jiayi.yu@epfl.ch

† E-mail: cheng.zhao@epfl.ch

‡ E-mail: albert.chuang@utah.edu

¹ <http://www.sdss.org/>

stein et al. 2011). It has collected the spectra of more than 1.5 million Luminous Red Galaxies (LRGs; Reid et al. 2016), the brightest red galaxies in the Universe. Its extended version, eBOSS (2014–2020; Dawson et al. 2016) in SDSS-IV (Blanton et al. 2017) has probed another 300,000 LRGs (Ross et al. 2020). Additionally, eBOSS has observed around 270,000 Emission Line Galaxies (ELGs; Raichoor et al. 2020). They are bluer, star-forming galaxies that are abundant in the redshift range of $0.5 < z < 2$, where there are active star formation processes (Madau et al. 1998). With such a big amount of tracers, both projects have achieved a percent-level precision in cosmological parameter measurements (Alam et al. 2017, 2021a). Ongoing surveys like the Dark Energy Spectroscopic Instrument (DESI, 2020–2025; DESI Collaboration et al. 2016) is expected to provide tracers in a larger footprint and with higher-resolution spectra, and reach a higher precision in scientific results.

Meanwhile, N -body simulations can solve numerically the gravitational evolution equation of DM in Λ CDM. They are able to accurately describe the DM distribution in the non-linear regime down to individual haloes in a large volume and provide halo properties at any cosmic epoch. Thus N -body simulations help validate cosmological theories that are based on perturbation theories across all the scales, and makes it possible to compare theoretical predictions with observations.

But there is a gap between dark-matter-only N -body simulations and observations. Since baryonic matter interacts with each other through all fundamental forces, their clustering properties do not necessarily follow those of DM on all scales (White & Rees 1978). Moreover, the spatial distributions of different types of galaxies, such as LRGs and ELGs, can also be different in the cosmic web (e.g., Malavasi et al. 2016; Kraljic et al. 2018). To bridge the gap, a galaxy–halo relation that modulates the clustering of haloes to match the observation is of great importance. Because it enables the direct comparison between the theory and the observation via simulation (Wechsler & Tinker 2018).

SubHalo Abundance Matching is a simple and intuitive empirical algorithm to model the galaxy–halo relation. As indicated by the name, SHAM makes use of DM haloes and their substructures that are dubbed subhaloes. The basic assumption of SHAM is a monotonic relation (not necessarily linear) between the galaxy luminosity (or stellar mass) and the halo mass (or the circular velocity; Kravtsov et al. 2004; Vale & Ostriker 2004; Nagai & Kravtsov 2005; Conroy et al. 2006; Behroozi et al. 2010). The algorithm applies the rank-ordering for both haloes and galaxies based on mass-related properties as just mentioned, and assigns galaxies to haloes/subhaloes one by one from the most massive end, until the SHAM galaxy catalogue reaches a desired number density.

Galaxies from this mock catalogue follow the observed or reconstructed luminosity function (e.g., Tasitsiomi et al. 2004; Conroy et al. 2006) or stellar mass function (e.g., Guo et al. 2010; Rodríguez-Torres et al. 2016) by construction. Their two-point statistics are tuned to be consistent with the observed one by introducing a Gaussian scatter between the galaxy luminosity and the halo circular velocity (Tasitsiomi et al. 2004) to include the scatter of the Tully–Fisher relation (Willick et al. 1997; Steinmetz & Navarro 1999). Using the peak maximum circular velocity throughout accumulation history (V_{peak}) instead of the halo mass further improves the performance of SHAM, since the galaxy accretion is free from the mass-stripping effect of subhaloes after reaching V_{peak} (Trujillo-Gomez et al. 2011). With all the improvements, SHAM catalogues of Rodríguez-Torres et al. (2016) predict the galaxy–halo relation that agrees with the weak-lensing observation from Shan et al. (2017). Other work on SHAM has also included the effect of halo

assembly bias and galaxy formation (e.g., Chaves-Montero et al. 2016; Contreras et al. 2021). Due to the single-parameter feature and its good agreement on data, SHAM has become a useful tool in cosmological studies.

While most of the SHAM studies choose to fit the projected 2PCF which marginalizes the effect along the line of sight, 2PCF multipoles can provide extra information in that direction. Due to the Redshift-Space Distortion (RSD), 2PCF quadrupole in the redshift space is vulnerable to the bias induced by the redshift uncertainty. This uncertainty mainly comes from the LRG redshift determination pipeline that uses broad absorption lines to determine the redshift (Bolton et al. 2012). For eBOSS LRG, Ross et al. (2020) find the uncertainty measured by the repeat observations can be fit by a Gaussian function with a dispersion of 91.8 km s^{-1} . This is negligible for large-scale clustering analysis like Baryon Acoustic Oscillation (BAO) at over $80 h^{-1} \text{ Mpc}$. Meanwhile, Smith et al. (2020) demonstrates that the redshift uncertainty of eBOSS quasars influences the quadrupole on $r < 60 h^{-1} \text{ Mpc}$, affecting SHAM that mainly employs 2PCF on $r < 40 h^{-1} \text{ Mpc}$.

Moreover, the standard SHAM algorithm described above works well for bright galaxies with complete samples, as it matches halo masses and galaxy masses starting from the most massive ones. When the sample is incomplete due to the survey requirement (e.g. exclude targets with higher luminosity) or when the tracer is absent in massive haloes due to the quenching process (e.g., Kauffmann et al. 2004; Dekel & Birnboim 2006), this implementation can be problematic (Favole et al. 2016a; Rodríguez-Torres et al. 2016).

In this paper, we present a general 3-parameter SHAM algorithm for LRGs on $5\text{--}25 h^{-1} \text{ Mpc}$ that considers the redshift uncertainty effects and the galaxy completeness. In Section 2, we describe the observational data, the N -body simulation and the galaxy mocks for covariance matrices. The calculation of 2PCFs and projected 2PCFs, the redshift uncertainty measurements, and the implementation of SHAM are introduced in Section 3. Section 4 illustrates the good performance of SHAM in fitting the 2PCF, reproducing the redshift uncertainty, the galaxy incompleteness evolution and the projected 2PCF of the observation. Finally, we summarize our findings in Section 5. In our study, we use a flat Λ CDM cosmology with $\Omega_m = 0.31$ and $H_0 = 67.7 \text{ km s}^{-1} \text{ Mpc}^{-1}$, and the line-of-sight direction of the comoving space is along the Z -axis.

The BOSS & eBOSS SHAM study is part of the final release of the eBOSS measurement. Ross et al. (2020); Lyke et al. (2020) describe in detail catalogues for the large-scale structure analysis. The mock challenge tasks are completed by Alam et al. (2021c); Avila et al. (2020a); Rossi et al. (2021); Smith et al. (2020) for systematics estimations. Galaxy mocks for covariance matrices used for cosmological analysis are constructed by Lin et al. (2020); Zhao et al. (2021a). The BAO and RSD measurements² are based on the clustering of LRGs at $0.6 < z < 1.0$ (Bautista et al. 2021; Gil-Marín et al. 2020), ELGs at $0.6 < z < 1.1$ (Raichoor et al. 2020; Tamone et al. 2020; de Mattia et al. 2021), quasars (QSOs) at $0.8 < z < 2.2$ (Hou et al. 2021; Neveux et al. 2020) and also the Ly α forest at $z > 2.1$ (du Mas des Bourboux et al. 2020). Their cosmological interpretations³ in combination with the final BOSS results and other probes can be found in Alam et al. (2021b). eBOSS

² <https://www.sdss.org/science/final-bao-and-rsd-measurements>

³ see <https://www.sdss.org/science/cosmology-results-from-eboss>, and https://svn.sdss.org/public/data/eBOSS/DR16cosmo/tags/v1_0_1/

data also permit the analysis with cosmic voids (Aubert et al. 2020) and multiple tracers (Wang et al. 2020; Zhao et al. 2021b, 2022).

2 DATA

2.1 SDSS Galaxies

We use the galaxy catalogues from the final data releases of SDSS-III BOSS (DR12; Alam et al. 2015) and SDSS-IV eBOSS (DR16 Ahumada et al. 2020). BOSS LRGs are composed of two sub-samples: LOWZ at $0.15 < z < 0.5$ and CMASS at $0.4 < z < 0.7$ (Reid et al. 2016). For eBOSS, its LRG sample has redshift at $0.6 < z < 1.0$ (Ross et al. 2020). Galaxy samples in the catalogues are pre-selected using the photometric information to ensure the observed samples are clean and abundant at a given redshift range for scientific targets. Their spectra are observed by fibers (York et al. 2000; Gunn et al. 2006; Smee et al. 2013) and processed by the spectroscopic pipeline in order to determine their galaxy type and redshifts (Aihara et al. 2011; Bolton et al. 2012). The catalogues used for clustering analysis (clustering catalogue hereafter) are composed of the 3D position of tracers, as well as several weights to eliminate systematics effects on 2PCF measurements.

2.1.1 Target Selection

Target selection using the photometric information includes the signal-to-noise ratio (SNR) selection, the colour selection, the flux limits cut, and the star exclusion (Reid et al. 2016; Prakash et al. 2016). In general, those criteria are meant to have high quality LRG spectra, obtain the designed redshift range and number density, exclude the low-redshift, blue galaxies and ensure high-redshift successful rate, and remove stars from LRG samples, respectively. LOWZ at $0.2 < z < 0.4$ and CMASS $z < 0.6$ are expected to be nearly volume-limited, i.e., they are complete (Reid et al. 2016). The study of Leauthaud et al. (2016) confirms the LOWZ completeness but also finds CMASS is not as complete as Reid et al. (2016) describes.

For eBOSS LRG, there is a special magnitude cut, namely

$$i \geq 19.9, \quad (1)$$

which is set to avoid the BOSS CMASS galaxies (Prakash et al. 2016). This lower limit corresponds roughly to an upper limit of the stellar mass, meaning that the most massive LRGs may have been excluded from the eBOSS samples. We use V_{ceil} to account for it and we will explain it in detail in Section 3.3.

2.1.2 Repeat Observations

Repeat observations from SDSS aim at testing the reproducibility of the spectral measurements and obtaining a higher SNR by coadding multiple spectra (Dawson et al. 2012). We use them to estimate the redshift uncertainty statistically in Section 3.2. The redshifts of repeated samples from BOSS are determined by IDLSPEC2D (Bolton et al. 2012) and those from eBOSS LRGs are determined by REDROCK⁴. Less than 5% of galaxies in the clustering catalogues are observed twice, but those galaxies are good representatives of the clustering galaxies (Section 4.2).

⁴ <https://github.com/desihub/redrock>

2.1.3 Galaxy Weights

The 2PCF contains the information of cosmological parameters and structure growth in its amplitude. But the amplitude can be easily modified by various systematics, e.g., photometric systematics, redshift failures, fibre collision effects and the varying galaxy number density at different redshift (Reid et al. 2016; Ross et al. 2020). The corresponding weights to remove their impacts are: w_{photosys} for all the photometric effects, w_{noz} for the redshift failure rate, w_{CP} for the missing close galaxy pairs due to the fibre collision and w_{FKP} for minimizing the cosmic variance.

The fibre collision problem arises from the physical size of fibres ($62''$) that defines the minimum separation between two fibres. Hence galaxies with small angular distances (i.e., close pairs) cannot be observed in a single exposure. For the BOSS data, the close-pair weight

$$w_{\text{CP}} = \frac{N_{\text{CP}} + N_{\text{good}}}{N_{\text{good}}}, \quad (2)$$

is applied to the nearest tracer of collided targets to nullify the fibre collision effects. Here N_{CP} is the number of the half-missing tracer pairs and N_{good} is the number of tracers with good redshifts (Ross et al. 2020). This nearest-neighbour approach is not able to fully correct the fibre collision effect (Guo et al. 2012; Rodríguez-Torres et al. 2016). Nevertheless, our SHAM fitting results are not biased by this effect (see Appendix A).

eBOSS uses a different weighting scheme. The pairwise-inverse-probability (PIP) weighting proposed by Bianchi & Percival (2017) is a better way to account for galaxy pairs with one missing in a single observation and the angular up-weighting (ANG) scheme introduced by Percival & Bianchi (2017) can recover missing galaxy pairs with a distance smaller than the size of a fibre. Mohammad et al. (2020) apply both PIP and ANG weights on eBOSS samples and provide unbiased galaxy clustering down to $0.1 h^{-1} \text{Mpc}$.

The FKP weight is obtained by (Feldman et al. 1994)

$$w_{\text{FKP}} = \frac{1}{1 + \bar{n}(z)P_0}, \quad (3)$$

where $\bar{n}(z)$ is the number density at redshift z and P_0 is the amplitude of the observed power spectrum at $k \approx 0.15 h \text{Mpc}^{-1}$. For LRGs in BOSS/eBOSS, we take $P_0 = 10000 h^{-3} \text{Mpc}^3$ (Reid et al. 2016; Ross et al. 2020).

2.2 N-body Simulation: UNIT

Future galaxy surveys will span to larger cosmological volumes with a deeper photometry. The resolution and effective volume of the N -body simulation should also keep up with the improvements. In our study, we use the Universe N -body simulations for the Investigation of Theoretical models from galaxy surveys⁵ (UNIT; Chuang et al. 2019). This is a high-resolution and large-effective-volume N -body simulation that uses the fixed-amplitude method to suppress the cosmic variance, thus increasing the effective volume (Angulo & Pontzen 2016). Its effective volume is over 10 times larger than that of BOSS/eBOSS LRGs. UNIT has 4096^3 particles in $1 h^{-3} \text{Gpc}^3$ cubic box, and a mass resolution of $1.2 \times 10^9 M_{\odot} h^{-1}$. Its cosmological parameters are $\Omega_m = 0.3089$, $h \equiv H_0/100 \text{km s}^{-1} \text{Mpc}^{-1} = 0.6774$, $n_s = 0.9667$, $\sigma_8 = 0.8147$. The simulation evolves from $a(t) = 0.01$ ($z = 99$) to $a(t) = 1$ ($z = 0$), and produces 128 snapshots at different redshifts. In our study, we use 12 snapshots from

⁵ <http://www.unitsims.org/>

$z = 0.2760$ to $z = 0.9011$ as shown in Table 1, and we take one simulation box in each snapshot given the large effective volume of UNIT (see Section 4.1).

2.3 Galaxy Mocks for Covariance Matrices

We use galaxy mocks to calculate covariance matrices in Section 3.4. For BOSS, we use 1200 DR12 PATCHY mocks in each galactic cap. For eBOSS, there are 1000 realizations of EZMOCCK mocks for LRGs in each galactic cap. Both of them are able to reproduce the observational two-point and three-point statistics down to non-linear scales.

Kitaura et al. (2014) introduces the PATCHY code to generate galaxy mocks based on the Augmented Lagrangian Perturbation Theory (ALPT). They determine the galaxy properties by apply their own SHAM to the BigMultiDark simulation⁶ (Klypin et al. 2016) and fit the observational statistics in both real and redshift space. The clustering properties of PATCHY mocks are then calibrated by those of SHAM catalogues. The fiducial cosmology is a Λ CDM cosmology with $\Omega_m = 0.307115$, $\Omega_b = 0.048206$, $h = 0.6777$, $\sigma_8 = 0.8225$, $n_s = 0.9611$ (Kitaura et al. 2016).

The Effective Zel’dovich approximation mock (EZMOCCK) proposed by Chuang et al. (2015) is another fast methodology to generate mock halo or galaxy catalogues, with the same cosmology as PATCHY mocks. EZMOCCK relies on the Zel’dovich approximation (Zel’dovich 1970) to calculate the displacement of DM particles at any redshift given their initial positions. Tracers are assigned in the density field using both the deterministic and the stochastic bias model (Zhao et al. 2021a). Besides covariance matrix calculations, we also use EZMOCCK mocks with and without systematics to study the impact of the biased 2PCF monopole on the projected 2PCF in Section 4.4.

3 METHODS

3.1 Galaxy Clustering

The 2PCF, denoted by ξ , measures the excess probability of finding a galaxy pair compared to a random distribution in a given volume. We use the Landy–Szalay estimator (LS; Landy & Szalay 1993) which minimises the variances of the measurements:

$$\xi_{\text{LS}} = \frac{\text{DD} - 2\text{DR} + \text{RR}}{\text{RR}}, \quad (4)$$

where galaxy–galaxy pairs (DD), random–galaxy pairs (DR) and random–random pairs (RR) are normalized by the total number of pairs. ξ and the pair counts can be calculated as a function of the pair separation s and the cosine of the angle between s and the line-of-sight (β), i.e., $\mu = \cos(\beta)$. By weighting the 2D $\xi(s, \mu)$ with Legendre polynomials $P_\ell(\mu)$, we obtain the 1D ξ multipoles as

$$\xi_\ell(s) = \frac{2\ell + 1}{2} \int_{-1}^1 \xi(s, \mu) P_\ell(\mu) d\mu. \quad (5)$$

In our study we only consider the monopole ξ_0 and quadrupole ξ_2 at $s \in [5, 25] h^{-1}$ Mpc. This is because scales larger than $25 h^{-1}$ Mpc are prone to imaging systematics (Huterer et al. 2013) while scales smaller than $5 h^{-1}$ Mpc are sensitive to fibre collision effects. Even with nearest-neighbour close-pair weights w_{CP} , the biases of the 2PCF quadrupole due to fibre collision effects can be as large as 3σ

at $\sim 5 h^{-1}$ Mpc (Guo et al. 2012; Rodríguez-Torres et al. 2016). To understand its influence on our SHAM results, we test a fitting range of $[10, 25] h^{-1}$ Mpc – which is only mildly affected by fibre collisions – for the BOSS data. It turns out that the SHAM constraints in this range are consistent with those on $s \in [5, 25] h^{-1}$ Mpc (see Appendix A). So we use the fitting range $s \in [5, 25] h^{-1}$ Mpc for all BOSS/eBOSS samples hereafter.

We use linear s bins with $1 h^{-1}$ Mpc interval, and 120 linear μ bins in the range of $[0, 1)$, for most of the 2PCF measurements in this work. Only for the eBOSS LRGs in different redshift bins, we have 8 logarithmic bins for ξ_0 and ξ_2 respectively.

ξ can also be measured as a function of the distance parallel (π) and perpendicular (r_p) to the line-of-sight. By integrating $\xi(r_p, \pi)$ with respect to π , one obtains the projected 2PCF as

$$w_p(r_p) = \int_{-\pi_{\text{max}}}^{\pi_{\text{max}}} \xi(r_p, \pi) d\pi. \quad (6)$$

We use 8 logarithmic bins for $r_p \in [5, 25] h^{-1}$ Mpc, but π_{max} will be changed according to our needs as introduced in Section 4.4. FCFC⁷ (Zhao et al. in preparation) and CORRFUNC Python module (Sinha & Garrison 2019; Sinha & Garrison 2020) are employed to calculate $\xi_\ell(s)$ and w_p . $\xi_\ell(s)$ of eBOSS are computed with PIP+ANG-weighted pair counts (Mohammad et al. 2020).

Our SHAM galaxy catalogue is built from an N -body simulation in a box, so we convert the position of SHAM galaxies from real space to redshift space before calculating the 2PCF with (Kaiser 1987)

$$Z_{\text{redshift}} = Z_{\text{real}} + \frac{v_{\text{pec}, Z}}{a(t)H(z)}, \quad (7)$$

where Z is the coordinate and z is the redshift, $v_{\text{pec}, Z}$ is the peculiar velocity along the Z -axis. The estimator used to calculate the SHAM 2PCF is the Peebles–Hauser estimator (Peebles & Hauser 1974)

$$\xi_{\text{PH}} = \frac{\text{DD}}{\text{RR}} - 1, \quad (8)$$

where galaxy–galaxy pairs (DD) is also normalized by the total number of pairs. The random–random (RR) counts follow the analytical expression:

$$\text{RR} = \frac{4\pi}{3} \frac{s_{\text{max}}^3 - s_{\text{min}}^3}{V_{\text{box}}} \frac{1}{N_\mu}, \quad (9)$$

where s_{max} and s_{min} are the boundaries of the separation bins, $V_{\text{box}} = 1 h^{-3} \text{Gpc}^3$ is the volume of the simulation box and $N_\mu = 120$ is the number of μ bins. We do not apply weights to SHAM galaxies as there are no observational systematics and radial selection. The $\xi_\ell(s)$ of SHAM galaxies is calculated by the built-in 2PCF calculator in our SHAM implementation code.

3.2 Redshift Uncertainty

The redshift uncertainty is an inevitable error while measuring the redshift. It mainly affects the quadrupole of our clustering measurements (Smith et al. 2020), since it can be regarded as random peculiar motions along the line-of-sight. As suggested in Bolton et al. (2012), the redshift determination pipeline is the primary source of the redshift uncertainty of SDSS LRGs, but it is not the dominant source. Hence, using the error given by the pipeline will underestimate the redshift uncertainty. As a result, we estimate it statistically via repeat observations.

⁶ <http://www.multidark.org/>

⁷ <https://github.com/cheng-zhao/FCFC>

The redshift difference between two measurements Δz can be converted to Δv that represents the radial motion as

$$\Delta v = \frac{\Delta z}{(1+z)c}, \quad (10)$$

where z is the redshift of one of measurements with `SPECPRIMARY` = 1. With jackknife errors, we fit all the Δv histograms with Gaussian distributions, obtaining the best-fitting dispersion $\sigma_{\Delta v}$, as illustrated in Fig. 1. We also quote their standard deviation, $\hat{\sigma}_{\Delta v}$, as a statistical estimate of the redshift uncertainty. In our SHAM algorithm, its clustering effect is quantified by v_{smear} .

3.3 SHAM Implementation

Recent SHAM studies (e.g., [Campbell et al. 2018](#); [Granett et al. 2019](#); [Contreras et al. 2021](#)) consistently choose V_{peak} to represent the halo mass of haloes and subhaloes. The subsequent the progress of the SHAM algorithm is to sort the galaxy stellar mass and $V_{\text{peak}}^{\text{scat}}$, which is obtained as

$$V_{\text{peak}}^{\text{scat}} = V_{\text{peak}} S_g, \quad (11)$$

where

$$S_g = 1 + \mathcal{N}(0, \sigma^2), \quad (12)$$

and match them one by one from the largest $V_{\text{peak}}^{\text{scat}}$ until the number density of SHAM galaxies equals to that of the observation. In Eq. (11), $\mathcal{N}(0, \sigma^2)$ represents a Gaussian random distribution centred on zero with σ^2 variance, where σ is the only free parameter in the SHAM. The choice of the Gaussian function is due to the fact that the Tully–Fisher relation, i.e., the galaxy–halo mass relation, has Gaussian distributed residuals ([Willick et al. 1997](#); [Steinmetz & Navarro 1999](#)). We assert

$$S_g = \exp(\mathcal{N}(0, \sigma^2)). \quad (13)$$

when the Gaussian scatter is negative. Nevertheless, it does not change the fitting results.

There are four prerequisites for the standard SHAM described above: 1) the cosmology of the simulation has to be close to the true one; 2) the simulation should have a good resolution to resolve the subhaloes down to the low-mass end and halo properties should be accurate; 3) the observed clustering measurements should be unbiased; 4) the observational stellar mass function (SMF) has to be complete in the massive end. If one of these prerequisites is missing, SHAM will not model the observed clustering signal accurately on all scales.

For eBOSS LRGs, there is a rough truncation of the stellar mass in the massive end (Section 2.1.1). A straightforward way to account for this massive-end incompleteness is to discard the most massive haloes. We introduce a new parameter V_{ceil} to remove the V_{ceil} per cent of the largest scattered V_{peak} (i.e., $V_{\text{peak}}^{\text{scat}}$). Since σ and V_{ceil} both modulate the amplitude of 2PCF monopole, they are degenerate.

The redshift uncertainty can add bias to the observed 2PCF quadrupole. Therefore, we introduce an extra Gaussian-random distribution $\mathcal{N}(0, v_{\text{smear}}^2)$ in the peculiar velocity of SHAM galaxies as

$$v_{\text{pec},Z}^{\text{scat}} = v_{\text{pec},Z} + \mathcal{N}(0, v_{\text{smear}}^2). \quad (14)$$

The target is to mimic the impact of the measured Gaussian redshift uncertainties in the redshift-space clustering as presented in Fig. 1.

To conclude, our 3-parameter SHAM implementation is as follows:

(i) Scatter the V_{peak} as suggested in Eq. (11) with

$$S_g = \begin{cases} 1 + \mathcal{N}(0, \sigma^2), & \mathcal{N}(0, \sigma^2) \geq 0 \\ \exp(\mathcal{N}(0, \sigma^2)), & \mathcal{N}(0, \sigma^2) < 0; \end{cases} \quad (15)$$

(ii) Sort $V_{\text{peak}}^{\text{scat}}$ and discard the most massive V_{ceil} per cent of haloes/subhaloes;

(iii) From the remaining catalogue, keep the N_{gal} -th largest $V_{\text{peak}}^{\text{scat}}$.

(iv) Assign galaxies in the centre of those haloes/subhaloes, and smear the peculiar velocities of galaxies along the line of sight with Eq. (14);

(v) Convert the galaxy coordinates from the real space to the redshift space using Eq. (7).

To model correctly the observed clustering, the redshift of the UNIT snapshot should be close to the effective redshift of the data computed with

$$z_{\text{eff}} = \frac{\sum z w^2}{\sum w^2}. \quad (16)$$

where w is the total galaxy weight. For eBOSS ([Ross et al. 2020](#)),

$$w = w_{\text{photosys}} w_{\text{FKP}} w_{\text{noz}} w_{\text{CP}}, \quad (17)$$

while for BOSS the total weight has a different form ([Reid et al. 2016](#))

$$w = w_{\text{photosys}} w_{\text{FKP}} (w_{\text{noz}} + w_{\text{CP}} - 1). \quad (18)$$

Then we apply SHAM on this snapshot to find the best-fitting parameters. Besides the 2PCF calculator mentioned in Section 3.1, our code also has a built-in MULTINEST sampler which will be introduced in Section 3.4.

The number of SHAM galaxies N_{gal} is determined by the observed effective number density n_{eff} in a given redshift range calculated as

$$n_{\text{eff}} = \sqrt{\frac{\int n(z)^2 dV}{\int dV}} = \sqrt{\frac{\int n(\chi)^2 \chi^2 d\chi}{\int \chi^2 d\chi}}, \quad (19)$$

where the second equality is due to $dV = A_{\text{eff}}((\chi + d\chi)^3 - \chi^3)/3 = A_{\text{eff}}\chi^2 d\chi + \mathcal{O}(d\chi^2)$, A_{eff} is the effective area of the footprint and χ is the comoving distance for an object at redshift z . The values are reported in Table 1.

3.4 SHAM Fitting

The SHAM best-fitting parameters are obtained by minimizing the χ^2 value (i.e., the maximum log-likelihood) between the SHAM and the observational 2PCF. The χ^2 for a given parameter set $\Theta = \{\sigma, v_{\text{smear}}, V_{\text{ceil}}\}$ is defined as

$$\chi^2(\Theta) = (\xi_{\text{data}} - \xi_{\text{model}}(\Theta))^T \mathbf{C}^{-1} (\xi_{\text{data}} - \xi_{\text{model}}(\Theta)), \quad (20)$$

where $\xi = (\xi_0, \xi_2)$ denotes the vector composed of the 2PCF monopole and quadrupole. The vectors ξ_{data} and ξ_{model} represent the data vector and the SHAM model 2PCF respectively. In particular, ξ_{model} is obtained by averaging the 2PCFs of 32 SHAM galaxy realizations generated using the same Θ with different random seeds. This operation reduces the SHAM statistical uncertainty. \mathbf{C} is the unbiased covariance matrix ([Hartlap et al. 2007](#)):

$$\mathbf{C}^{-1} = \mathbf{C}_s^{-1} \frac{N_m - N_s - 2}{N_m - 1}, \quad (21)$$

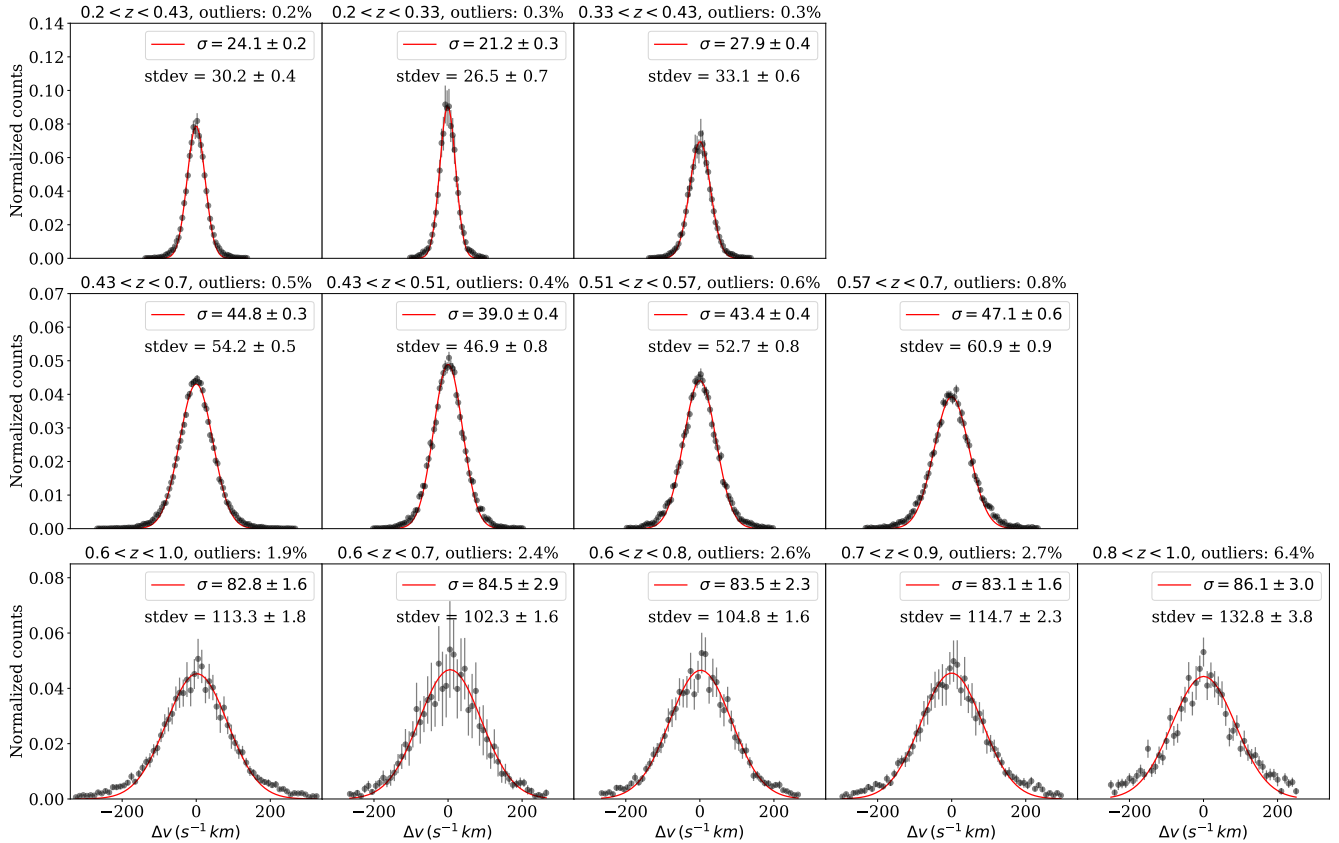


Figure 1. The Gaussian fitting of the Δv histograms. The error bars of Δv histograms are calculated from jackknife re-sampling. The best-fitting Gaussian models are shown in red lines, labelled with their dispersion values $\sigma_{\Delta v}$. The standard deviations of Δv is written below the legend and the proportion of outliers that are beyond the Gaussian fitting range is indicated above the subplots. SDSS has a Gaussian Δv histogram, and the outlier rate of eBOSS are much larger than those of BOSS, consistent with the difference between $\sigma_{\Delta v}$ and $\hat{\sigma}_{\Delta v}$.

where N_s is the length of ξ_{data} , i.e., the total number of bins used in the 2PCF fitting, and N_m is the number of mocks used to compute the covariance matrix. $N_m = 1200$ for BOSS PATCHY mocks and $N_m = 1000$ for eBOSS EZMOCK mocks. C_s is the covariance matrix calculated as (Zhao et al. 2021a)

$$C_{s,ij} = \frac{1}{N_m - 1} \sum_{k=1}^{N_m} [\xi_k(s_i) - \bar{\xi}(s_i)][\xi_k(s_j) - \bar{\xi}(s_j)], \quad (22)$$

where ξ_k is the correlation function measured from the k_{th} mock, and $\bar{\xi}(s_i)$ is the average of the mock correlation function in a given distance bin s_i .

We assume a Gaussian likelihood $\mathcal{L}(\Theta)$ for our parameters, which is

$$\mathcal{L}(\Theta) \propto e^{-\frac{\chi^2(\Theta)}{2}}, \quad (23)$$

and employ a Monte-Carlo sampler MULTINEST⁸ (Feroz & Hobson 2008; Feroz et al. 2009, 2019), an efficient nested sampling technique especially for multi-modal posteriors, to constrain Θ . The survival volume (i.e., the prior volume) is defined as (Feroz & Hobson 2008)

$$X(\lambda) = \int_{\{\Theta: \mathcal{L}(\Theta) > \lambda\}} \Pr(\Theta|H) d\Theta, \quad (24)$$

where $\Pr(\Theta|H)$ is the parameter prior, and the evidence integral can be written as

$$\mathcal{Z} = \int_0^1 \mathcal{L}(\Theta) dX \approx \sum_{i=1}^M \mathcal{L}_i w_i, \quad (25)$$

where i is the number of iterations, $w_i = \frac{1}{2}(X_{i-1} - X_{i+1})$, and X_i is a sequence of decreasing values as $0 < X_M < \dots < X_2 < X_1 < X_0 = 1$. During the sampling, live points walk randomly and simultaneously in the parameter space confined by the prior, and some of them will be deactivated if they have the lowest likelihood \mathcal{L}_i . The sampling terminates if the evidence contribution from the j_{th} iteration $\Delta \mathcal{Z}_j = \mathcal{L}_{\text{max}} X_j$ is lower than a certain threshold (i.e., the tolerance), where \mathcal{L}_{max} is the maximum likelihood among the current set of live points (Feroz et al. 2019). The final results of our SHAM do not change much when changing the tolerance and the initial number of live points. Therefore, for all the tests, we set the tolerance to be 0.5 and the number of particles to be 200, in order to improve the efficiency of the convergence.

The built-in analyser of PYMULTINEST⁹ (Buchner et al. 2014) is used to extract the median value and the 1σ limits of the parameters, and the maximum-likelihood χ^2 listed in Table 1. The parameter

⁸ <https://github.com/farhanferoz/MultiNest>

⁹ <https://github.com/JohannesBuchner/PyMultiNest>

project	redshift range	z_{eff}	z_{UNIT}	V_{eff} ($h^{-3} \text{ Gpc}^3$)	$10^4 n_{\text{eff}}$ ($h^3 \text{ Mpc}^{-3}$)	σ	v_{smear} ($\text{s}^{-1} \text{ km}$)	V_{ceil} (%)	χ^2/dof	rescaled χ^2/dof
LOWZ	$0.2 < z < 0.33$	0.2754	0.2760	0.29	3.37	$0.09^{+0.06}_{-0.06}$	$100.3^{+7.6}_{-10.4}$	$0.0067^{+0.0019}_{-0.0025}$	32/37	31/37
						$0.27^{+0.02}_{-0.02}$	$66.1^{+8.2}_{-9.8}$	/	33/38	32/38
LOWZ	$0.33 < z < 0.43$	0.3865	0.3941	0.33	2.58	$0.20^{+0.05}_{-0.05}$	$73.9^{+12.2}_{-12.3}$	$0.0059^{+0.0026}_{-0.0028}$	51/37	50/37
						$0.34^{+0.02}_{-0.01}$	$30.5^{+16.7}_{-16.2}$	/	54/38	52/38
CMASS	$0.43 < z < 0.51$	0.4686	0.4573	0.47	3.42	$0.30^{+0.05}_{-0.08}$	$45.0^{+20.6}_{-16.6}$	$0.0078^{+0.0074}_{-0.0040}$	41/37	39/37
						$0.43^{+0.01}_{-0.02}$	$17.4^{+11.8}_{-9.6}$	/	45/38	43/38
CMASS	$0.51 < z < 0.57$	0.5417	0.5574	0.46	3.63	$0.23^{+0.04}_{-0.04}$	$23.2^{+18.5}_{-15.0}$	$0.0144^{+0.0037}_{-0.0036}$	43/37	41/37
						$0.42^{+0.02}_{-0.01}$	$6.4^{+6.2}_{-4.0}$	/	60/38	58/38
CMASS	$0.57 < z < 0.7$	0.6399	0.6281	0.65	1.60	$0.17^{+0.13}_{-0.02}$	$73.1^{+8.2}_{-25.3}$	$0.0459^{+0.0029}_{-0.0143}$	54/37	51/37
eBOSS	$0.6 < z < 0.7$	0.6518	0.6644	0.16	0.939	$0.58^{+0.29}_{-0.22}$	$100.4^{+12.3}_{-12.8}$	$0.0510^{+0.0324}_{-0.0194}$	16/13	16/13
eBOSS	$0.6 < z < 0.8$	0.7071	0.7018	0.33	0.886	$0.38^{+0.31}_{-0.13}$	$98.8^{+10.8}_{-13.4}$	$0.0617^{+0.0185}_{-0.0308}$	24/13	23/13
eBOSS	$0.7 < z < 0.9$	0.7968	0.8188	0.26	0.647	$0.09^{+0.17}_{-0.04}$	$128.5^{+9.5}_{-22.2}$	$0.0690^{+0.0044}_{-0.0172}$	30/13	30/13
eBOSS	$0.8 < z < 1.0$	0.8778	0.9011	0.09	0.301	$0.22^{+0.17}_{-0.14}$	$134.2^{+18.5}_{-20.1}$	$0.0481^{+0.0153}_{-0.0155}$	16/13	16/13
LOWZ	$0.2 < z < 0.43$	0.3441	0.3337	0.62	2.95	$0.22^{+0.03}_{-0.05}$	$76.6^{+10.2}_{-8.2}$	$0.0031^{+0.0023}_{-0.0015}$	45/37	42/37
						$0.30^{+0.01}_{-0.01}$	$54.5^{+6.9}_{-6.7}$	/	45/38	42/38
CMASS	$0.43 < z < 0.7$	0.5897	0.5924	1.58	2.64	$0.20^{+0.20}_{-0.03}$	$63.5^{+9.1}_{-44.6}$	$0.0269^{+0.0032}_{-0.0190}$	81/37	70/37
eBOSS	$0.6 < z < 1.0$	0.7781	0.7018	0.43	0.626	$0.40^{+0.19}_{-0.06}$	$109.7^{+8.0}_{-6.1}$	$0.0542^{+0.0067}_{-0.0196}$	35/37	33/37

Table 1. Properties of analysed galaxy samples and their best-fitting SHAM results. The first six columns are the project names of galaxy samples, their redshift ranges, effective redshifts z_{eff} , the closest redshifts of the UNIT snapshot to z_{eff} , effective volumes, and their average number densities. The next four columns are the constraints of SHAM parameters (σ , v_{smear} , V_{ceil}) and the minimum χ^2/dof . The final column is the rescaled χ^2/dof taking into account the uncertainty of UNIT simulations. There are redshift bins with two sets of SHAM parameters. The first set (row) is from the 3-parameter SHAM and the second set is from 2-parameter SHAM without V_{ceil} . The 2-parameter SHAM can only be applied to complete samples, i.e., LOWZ and CMASS galaxies at $z < 0.6$ (Leauthaud et al. 2016). Redshift bins with only one set of SHAM results are from the 3-parameter SHAM.

set with the maximum-likelihood χ^2 is indicated in the posteriors provided by GETDIST (Lewis 2019) in Appendix C.

4 RESULTS

4.1 Galaxy Clustering Fitting

We calibrate our SHAM model with LRGs on $5\text{--}25 h^{-1} \text{ Mpc}$ for the full LOWZ, CMASS and eBOSS LRG samples as well as 9 finer redshift bins as summarized in Table 1. Figures 2–4 show that 2PCFs of the SHAM catalogues agree with those of the observational data in general. Note that there are 32 realizations of SHAM catalogues produced by the maximum-likelihood parameter set, aiming at reducing the statistical error brought by the Gaussian scatters. For this reason, we choose the mean value of their 2PCFs to be the SHAM 2PCF, and rescale their 2PCF standard deviations by $1/\sqrt{32}$ to obtain the error of the SHAM. We find that the SHAM error is negligible compared to observed statistical error determined by PATCHY mocks or EZMOCCK mocks. Thus, we decided to ignore it in this study.

The reduced χ^2 values from the fits do not include cosmic variances of the UNIT simulations. To include their influence in the analysis, we divide the reduced χ^2 by

$$\frac{\epsilon_{\text{com}}^2}{\epsilon_{\text{obs}}^2} = 1 + \frac{\epsilon_{\text{UNIT}}^2}{\epsilon_{\text{obs}}^2} \approx 1 + \frac{V_{\text{eff,obs}}}{V_{\text{eff,UNIT}}}, \quad (26)$$

where ϵ_{obs}^2 and ϵ_{UNIT}^2 represent the observational variance and the

cosmic variance of UNIT simulation respectively and ϵ_{com}^2 is the combination of two errors. $V_{\text{eff,obs}}$ is the effective volume calculated with (Wang et al. 2013; Reid et al. 2016)

$$V_{\text{eff,obs}} = \sum_i \left(\frac{\bar{n}(z_i) P_0}{1 + \bar{n}(z_i) P_0} \right)^2 \Delta V(z_i), \quad (27)$$

where $\Delta V(z_i)$ is the volume of the shell at redshift z_i and $\bar{n}(z_i)$ is the mean number density of that shell. The values are listed in the fourth column of Table 1 and we assume $V_{\text{eff,UNIT}} = 10 h^{-3} \text{ Gpc}^3$ (Chuang et al. 2019). The rescaled χ^2 values are recorded in the final column of Table 1. As the rescaled value is a better indicator of the goodness of the fit than the χ^2 value, our discussions hereafter are all based on the rescaled ones.

The χ^2 value for the bulk CMASS sample is relatively large compared to those of CMASS redshift slices and other bulk samples. This can be attributed to the varying sample completeness of CMASS sample which we will prove later in this chapter. The 2PCF quadrupoles of all CMASS SHAM samples are underestimated on $18\text{--}25 h^{-1} \text{ Mpc}$, which is consistent with the results of Rodríguez-Torres et al. (2016). Similar (but less obvious) discrepancies are also observed from the eBOSS samples. They may be due to some uncorrected systematics. The monopole disagreement on $r > 10 h^{-1} \text{ Mpc}$ and the resulting large χ^2 value for eBOSS SHAM at $0.7 < z < 0.9$ might be due to observational systematics as well.

Our measured $\sigma \in [0.17, 0.40]$ for CMASS at $0.43 < z < 0.7$ is consistent with $\sigma = 0.31$ obtained by Rodríguez-Torres et al. (2016). It is worth noting that their scatter considers the incompleteness of the observed stellar mass function, i.e., they obtain the

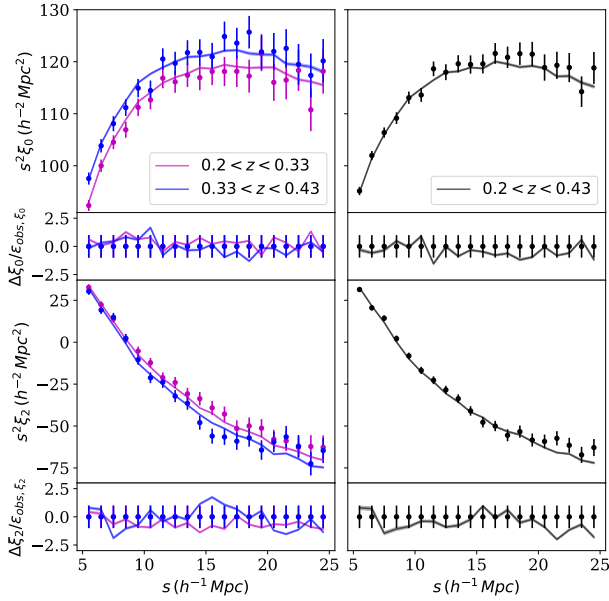


Figure 2. The best-fitting 3-parameter SHAM 2PCF multipoles compared with those of the LOWZ observations on 5–25 h^{-1} Mpc. The observational data and the cosmic variance $\epsilon_{\text{obs},\xi_{0,2}}$ are represented by dots with error bars. Solid lines with shades are SHAM 2PCFs and their errors. The first and third row are the monopole and the quadrupole respectively. Residuals normalized by $\epsilon_{\text{obs},\xi_{0,2}}$ are shown in the second and fourth row. The left column is for galaxy samples in redshift slices and the right column is for those in the bulk redshift range. SHAM 2PCFs agree with the observations with rescaled reduced χ^2 values around 1.

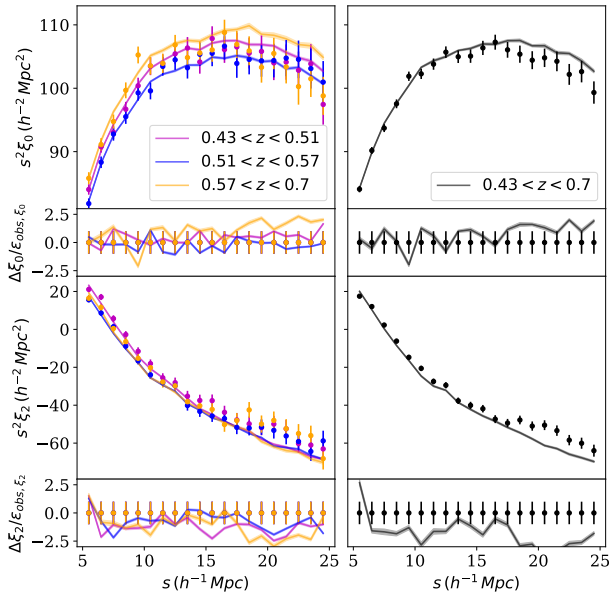


Figure 3. Same figure as Fig. 2, but for CMASS LRGs. The deviation for the bulk CMASS sample (right panels) is relatively large compared to those of the sliced redshift bins. We attribute this difference to its inhomogeneous sample completeness shown in Section 4.1.

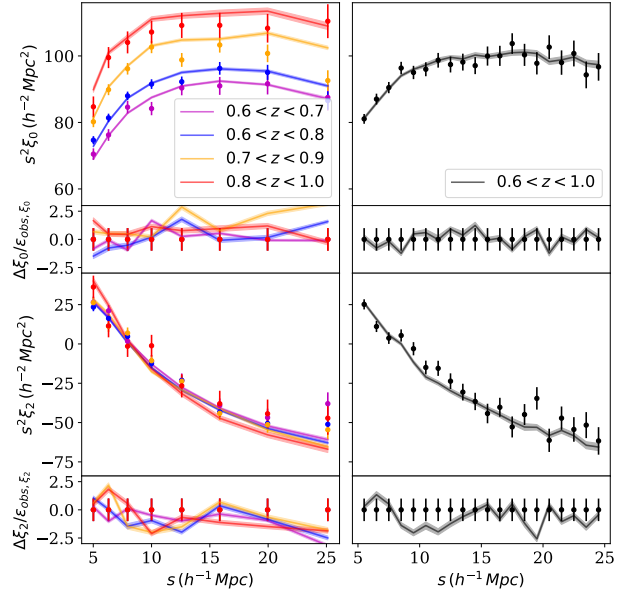


Figure 4. Same figure as Fig. 2, but for eBOSS LRGs. The SHAM 2PCFs also agree with the observations except the one at $0.7 < z < 0.9$.

intrinsic scatter σ_{int} . But we assume that the observed stellar mass function in a certain range is complete. It means that our σ account for both the intrinsic scatter and the observed incompleteness.

Since BOSS samples are complete at $z < 0.6$ (Reid et al. 2016; Leauthaud et al. 2016), we also apply our SHAM model without V_{ceil} (2-parameter SHAM hereafter) to the same simulation snapshot as the 3-parameter version and fit to the same data. The best-fitting 2PCFs and parameter constraints are shown in Fig. 5 and Table 1 respectively. The rescaled reduced χ^2 values for the 2- and 3-parameter SHAM models are similar for all LOWZ LRGs and CMASS LRGs at $0.43 < z < 0.51$, which confirms their galaxy completeness. The reduced χ^2 for the 2-parameter SHAM at $0.51 < z < 0.57$ is significantly larger (the χ^2 difference shows that SHAM with $V_{\text{ceil}} = 0$ is rejected more than 4σ), due to the discrepancy of quadrupole on $5\text{--}7 h^{-1}$ Mpc. It also means σ and V_{ceil} are not completely degenerate. The monopole of the best-fitting 2-parameter SHAM is also systematically lower than that of the observation. The issue in the result of the 2-parameter SHAM demonstrate that CMASS at $0.51 < z < 0.57$ is not complete, i.e., $V_{\text{ceil}} \neq 0$, contrary to what has been presented in Reid et al. (2016). This is consistent with the marginalized posterior distributions of V_{ceil} in the 3-parameter SHAM (see Fig. C4).

4.2 Redshift Uncertainty indicated by v_{smear}

Fig. 6 shows that $\hat{\sigma}_{\Delta v}$ increases monotonically with z_{eff} . This is consistent with the fact that the absorption lines used to determine the redshift are broader at higher redshift than those at lower redshift, leading to larger redshift uncertainties. There is a general consistency between the best-fitting SHAM v_{smear} and $\hat{\sigma}_{\Delta v}$, $\sigma_{\Delta v}$ for CMASS. For the eBOSS samples, SHAM v_{smear} agrees with $\hat{\sigma}_{\Delta v}$, but both of them are systematically larger than $\sigma_{\Delta v}$. It means that we cannot neglect the Gaussian-fitting outliers and their effects on eBOSS quadrupoles. The tail of eBOSS Δv distributions also slightly deviates from the Gaussian model, meaning that eBOSS $\sigma_{\Delta v}$ is not a good representative of the observed

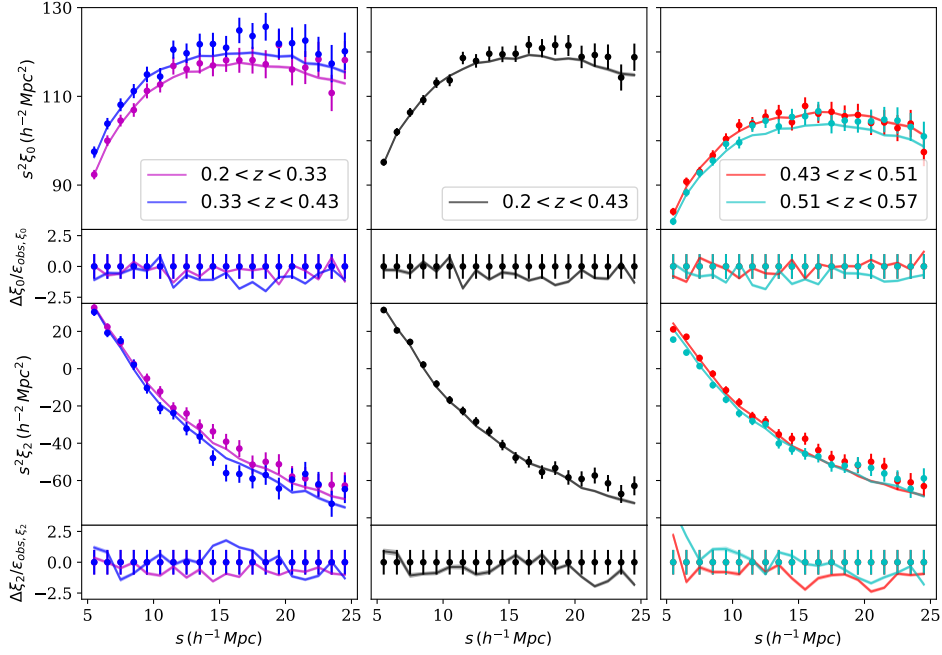


Figure 5. 2PCF multipoles of the best-fitting 2-parameter SHAM (with σ and v_{smear}) compared with those of the observations on $5\text{--}25 h^{-1} \text{Mpc}$ as in Fig. 2. The first column is for LOWZ in redshift slices, the second column is for LOWZ at a bulk redshift range, and the third column is for CMASS in redshift slices. SHAM 2PCF at $z < 0.51$ agrees with the observational 2PCF. However, a significant difference in the first two bins of the quadrupole is shown for the CMASS sample at $0.51 < z < 0.57$.

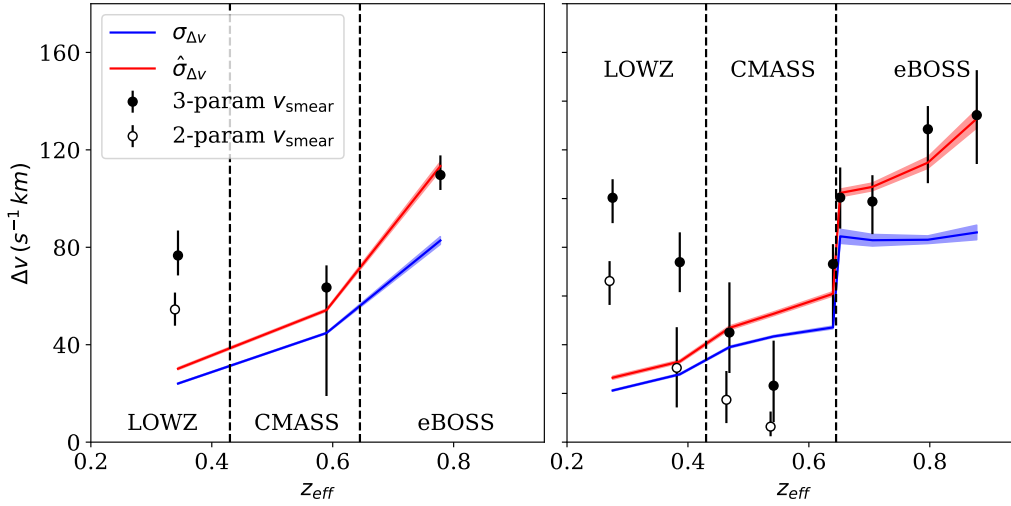


Figure 6. Comparison between the measured v_{smear} from the 3-parameter SHAM (black dots with error bars) and that from the 2-parameter SHAM (open circles with error bars; a horizontal offset is applied to avoid overlapping), the best-fitting Gaussian dispersion $\sigma_{\Delta v}$ (blue line with shades) and the standard deviations $\hat{\sigma}_{\Delta v}$ (red lines with shades) of the Δv distribution. The left panel is for the entire sample, while the right panel is for samples in redshift slices. Both the BOSS CMASS sample and the eBOSS LRG sample show good agreements between v_{smear} values and the redshift uncertainties measured from repeat samples. However, for the BOSS LOWZ sample, v_{smear} values are significant larger than those estimated from repeat observations.

redshift uncertainty. The best-fitting v_{smear} values of 2-parameter SHAM are lower than those of the 3-parameter SHAM, and this difference is larger for complete samples at $z < 0.51$ than that of CMASS at $0.51 < z < 0.57$. This is not a contradiction because the biggest change in $\sigma\text{--}v_{\text{smear}}$ posterior happens in CMASS at $0.51 < z < 0.57$ as shown in Figures C7–C9. The small change in v_{smear} is due to its weaker $V_{\text{ceil}}\text{--}v_{\text{smear}}$ degeneracy.

Discrepancies also exist for LOWZ LRGs at all redshifts and they remain for the 2-parameter LOWZ SHAM. To compare the differences in the quadrupole, we replace the best-fitting v_{smear} values with $\sigma_{\Delta v}$, generate SHAM galaxy catalogues and calculate the 2PCFs. As presented in Fig. 7, their quadrupole differences are larger than 3σ . It means that besides the statistical redshift

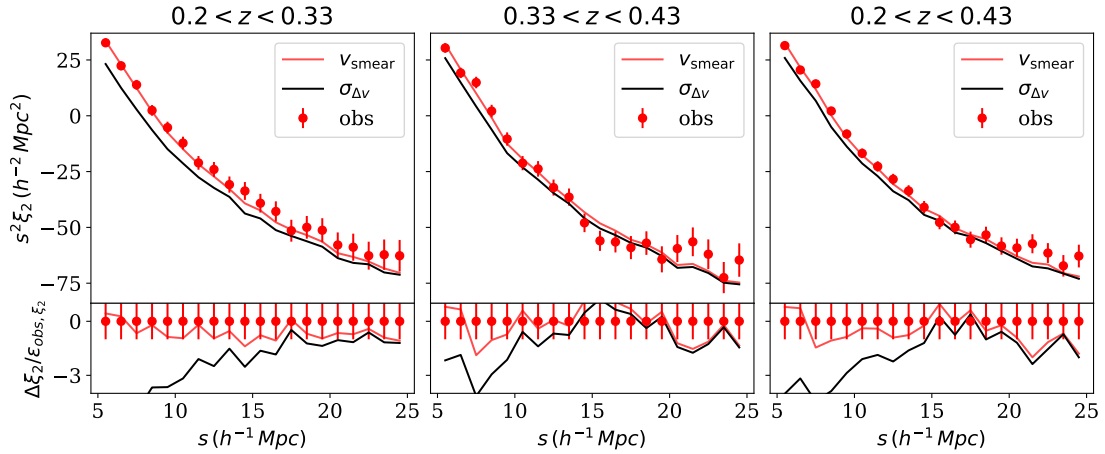


Figure 7. Comparison among the quadrupoles from the observation (red dots with error bars), the best-fitting SHAM (red lines), and the SHAM 2PCF obtained by replacing the best-fitting v_{smear} with $\sigma_{\Delta v}$ (black lines). The first, second and third column represents LOWZ samples at $0.2 < z < 0.33$, $0.33 < z < 0.43$ and $0.2 < z < 0.43$, respectively. The differences between two quadrupoles on $r < 10 h^{-1} \text{Mpc}$ are mostly larger than 3σ .

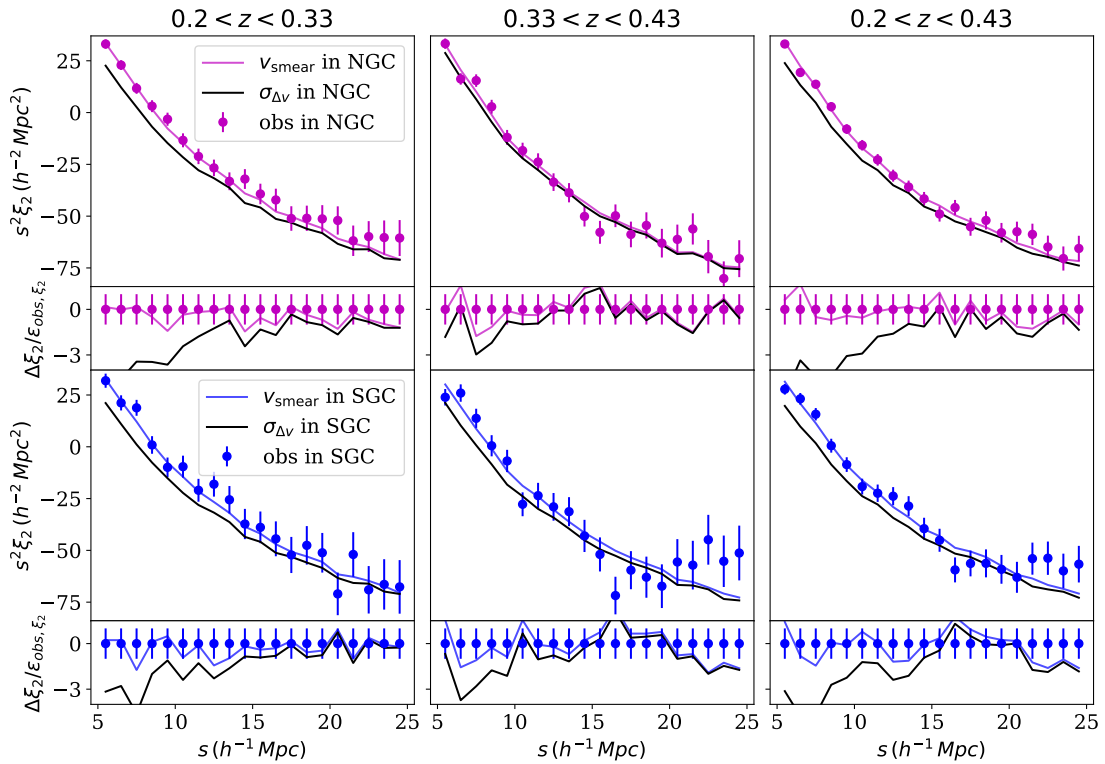


Figure 8. Same as Fig. 7, but using the LOWZ NGC sample (magenta lines) and LOWZ SGC sample (blue lines) separately. The discrepancies between v_{smear} and $\sigma_{\Delta v}$ are not mitigated for LOWZ SGC when there is a high rate of SDSS-III sample.

uncertainty, LOWZ has unknown factors that boost the quadrupole. We investigate various potential causes listed below.

A. Missing subhaloes or velocity bias in the simulation:

The host haloes/subhaloes for LRGs have a large mass (e.g. > 1000 particles), so we expect they are well resolved. But their peculiar velocity might have biases especially for subhaloes. However, our simulation-based SHAM provides v_{smear} that agrees with CMASS and eBOSS samples and we do not expect a significant evolution in the velocity bias. Therefore, the properties of haloes and subhaloes

should be reliable and do not lead to the v_{smear} disagreement in LOWZ.

B. Observational systematics:

The LOWZ sample includes SDSS-I/II galaxies with a redshift determination pipeline different from that of SDSS-III BOSS (Bolton et al. 2012). Thus, it is possible that the spectroscopic pipelines yield different uncertainties of redshift measurements. In fact, we find that in the clustering catalogue, 56 per cent of galaxies in the North Galactic Cap (NGC) and 90 per cent of galaxies in the South Galactic Cap (SGC) are from

SDSS-III. The component difference in two galactic caps indicates that we can analyse NGC and SGC separately. Repeated samples are all from SDSS-III. Therefore, the Δv from repetitive observations may not be representative of the redshift uncertainty of the LOWZ clustering.

However, as shown in Fig. 8, a high proportion of SDSS-III galaxies in the SGC does not mean a smaller difference between the $\sigma_{\Delta v}$ -generated 2PCF and the v_{smear} -generated 2PCF compared to the difference for LOWZ in the NGC. Therefore, the difference in the two spectroscopic pipelines cannot explain the v_{smear} discrepancy.

C. Underestimation of redshift uncertainties: Considering the fact that errors from the spectroscopic pipeline underestimate redshift uncertainties, it is difficult to directly prove the representative of samples from the repeat observation. Nevertheless, we can proceed with the photometric information (Appendix B). In the LOWZ sample, we find that the fraction of the blue samples f_{blue} in repeat observation is smaller than that of the clustering sample, but the differences are minor (See Table B1 and Table B2). Given the similarity in the f_{blue} and colour–redshift distributions, the sample of the repeat observations are unbiased representatives of galaxies in the clustering catalogue. Even if the repeated samples are biased, this is not the main cause of the discrepancy. Because the redshift uncertainty of LOWZ at lower redshift should be smaller than that of CMASS, but v_{smear} of LOWZ is systematically larger than that of CMASS.

D. A more complete model for galaxy assignment: While we are using the same model for CMASS and eBOSS LRGs to describe LOWZ, the discrepancy might indicate that a more complete model is required. E.g., the LOWZ sample is composed of a different type of galaxies which has more satellites than CMASS.

In fact, our satellite fraction (f_{sat}) for LOWZ at $0.2 < z < 0.43$ is 12.6 per cent, similar to CMASS $f_{\text{sat}} = 12.3$ per cent at $0.43 < z < 0.7$. They are close to results from Halo Occupation Distribution fitting with w_p , another empirical model for the galaxy–halo relation: Parejko et al. (2013) based on DR9 give 12 ± 2 per cent for LOWZ at $0.2 < z < 0.4$ and Reid et al. (2014) based on DR10 give 10 ± 2 per cent at $0.43 < z < 0.7$. Both SHAM and HOD do not support the explanation of large f_{sat} in LOWZ. Nevertheless, given the difference in data and fitting scales, f_{sat} can still be the explanation. Additionally, as pointed out by Ross et al. (2014) and Favole et al. (2016b), we know that the blue tail of CMASS galaxies show a higher quadrupole at $5\text{--}40 h^{-1}$ Mpc compared to the dominating redder galaxies, which has 2PCF close to that of the full catalogue. For LOWZ, the ad hoc blue galaxies might play a more important role in the clustering properties. The velocity bias is also found to be different in CMASS and LOWZ samples (Guo et al. 2015; Lange et al. 2022). So it is possible that the LOWZ discrepancy can be mitigated by a better model that considers those factors. We leave it for a future work.

4.3 Galaxy Incompleteness indicated by σ and V_{ceil}

Due to the high degeneracy between σ and V_{ceil} , the redshift evolutions of σ and V_{ceil} are not obvious in the marginalized posterior of eBOSS (Fig. C6). But the 2D σ – V_{ceil} posterior contours show a clear trend that σ or V_{ceil} are smaller at higher redshift.

Thus, given a smaller σ , we keep more haloes with large V_{peak} that can be scattered to a certain range of $V_{\text{peak}}^{\text{scat}}$, leading to a smaller stellar mass incompleteness (see Section 4.1). A smaller V_{ceil} means to remove fewer haloes with the largest $V_{\text{peak}}^{\text{scat}}$, so the sample is more complete at massive-end. This agrees with the minimum magni-

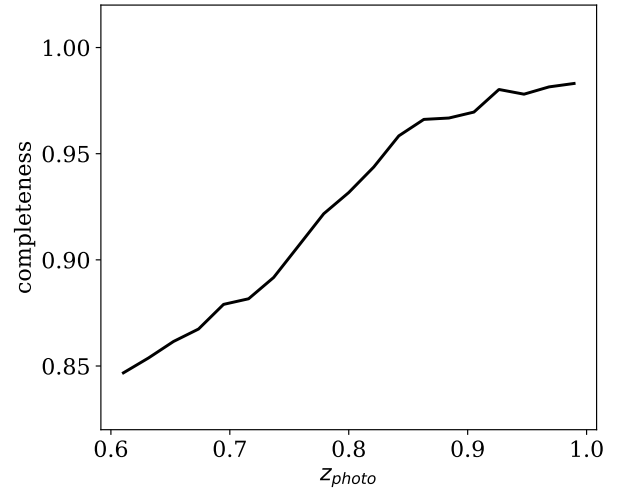


Figure 9. The redshift evolution of the completeness of eBOSS LRG targets. The photometric redshifts (z_{photo}) are taken from the DECaLS DR9 catalogues. The increasing completeness with respect to the redshift is the result of the i-band lower limit imposed in the LRG target selection.

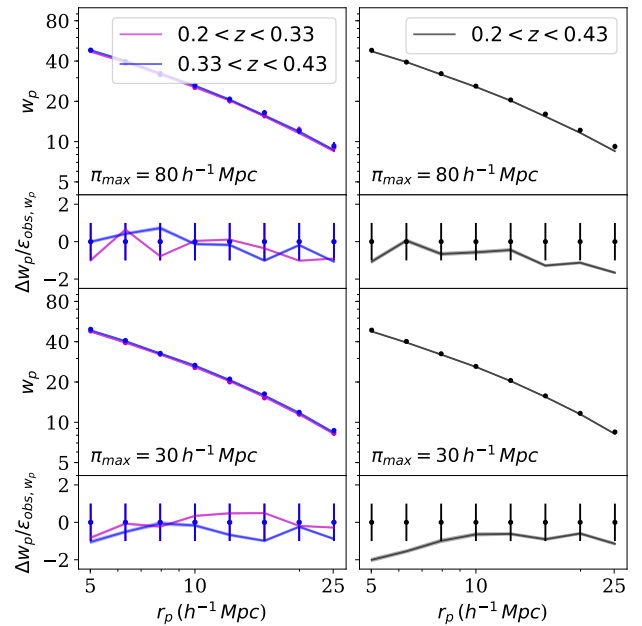


Figure 10. The w_p comparison between the best-fitting SHAM catalogues and the observations. The first row and the third row are w_p with π integrating up to $80 h^{-1}$ Mpc and $30 h^{-1}$ Mpc respectively, and their residuals normalized by the cosmic variance $\epsilon_{\text{obs}, w_p}$ is shown in the second and fourth row. π_{max} in the figures is for both observational and SHAM galaxies. The deviation at r_p around $20 h^{-1}$ Mpc for the bulk sample ($0.2 < z < 0.43$) decreases while using a smaller π_{max} . However, we see that the deviation at $5 h^{-1}$ Mpc increases which might indicate systematics at smaller scales.

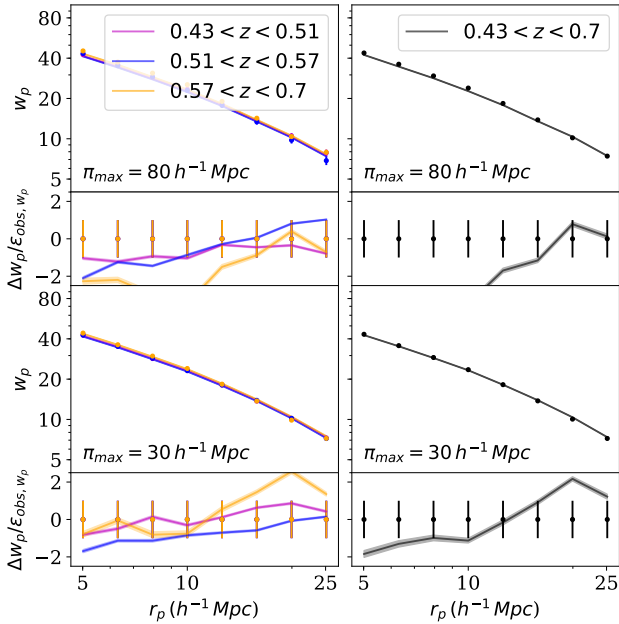


Figure 11. Same as Fig. 10, but for CMASS LRGs. SHAM catalogues start to be more consistent with the observed w_p with $\pi_{\max} = 30 h^{-1} \text{ Mpc}$ compared to $\pi_{\max} = 80 h^{-1} \text{ Mpc}$. Large deviations are found in the case of $\pi_{\max} = 80 h^{-1} \text{ Mpc}$. This is consistent with our findings from multipoles which indicate systematics at larger scales, e.g. $r > 18 h^{-1} \text{ Mpc}$.

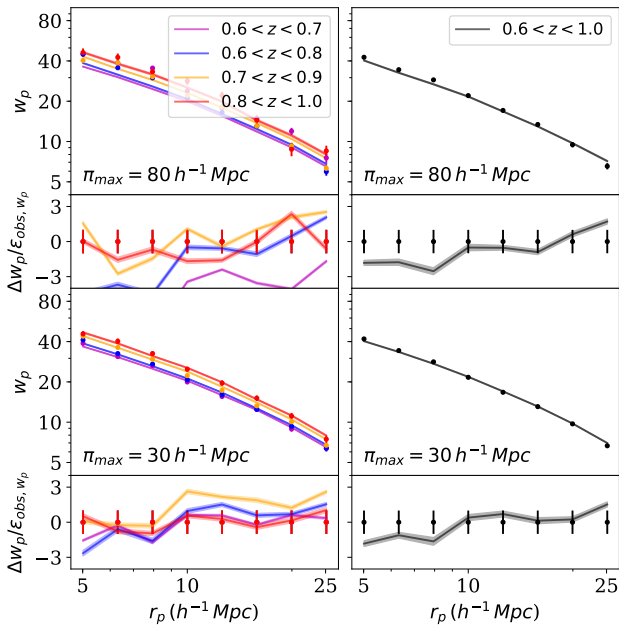


Figure 12. Same as Fig. 10, but for eBOSS LRGs. Left figures (small redshift bins) show obvious deviations when using $\pi_{\max} = 80 h^{-1} \text{ Mpc}$, but the deviations are mitigated when using $\pi_{\max} = 30 h^{-1} \text{ Mpc}$.

tude truncation mentioned in Section 2.1.1, since this threshold is expected to remove fewer galaxies at higher redshift (Zhai et al. 2017). To demonstrate this, we plot the completeness–redshift relation in Fig. 9. The completeness is defined as the ratio of the number of eBOSS LRG targets with a complete target selection including (Prakash et al. 2016), to that from a target selection without the i -band lower limit $i \geq 19.9$ (Eq. (1)). Since there are no spectroscopic redshift measurements for objects excluded by the eBOSS target selection criteria, we match the eBOSS target catalogues with the DECaLS DR9 data¹⁰ (Dey et al. 2019) to make use of the DECaLS photometric redshift measurements (Zhou et al. 2020) and 78.5 per cent of the eBOSS LRG candidates without the i -band lower limit are found in the DECaLS catalogue.

For the complete samples, i.e., LOWZ and CMASS at $0.43 < z < 0.51$, we obtain much tighter constraints on σ at different redshifts, as shown in Table 1. Since the σ parameter in this study absorbs the incompleteness of stellar mass function, our measurements provide upper bounds of the intrinsic scatter between stellar mass and our halo mass proxy V_{peak} , i.e. $\sigma_{\text{int}} < 0.31$ at $0.2 < z < 0.33$, $\sigma_{\text{int}} < 0.36$ at $0.33 < z < 0.43$, and $\sigma_{\text{int}} < 0.46$ at $0.43 < z < 0.51$ with 95 percent confidence. We do not consider the measurement at $0.51 < z < 0.57$ to be robust as explained in Section 4.1.

4.4 Consistency Check with w_p

In principle, when the 2PCF multipoles of a SHAM catalogue agree well with those of the corresponding observational data, the w_p of the two catalogues should also be consistent. To investigate the impacts of potential systematic effects that are usually observed on large scales (Ross et al. 2016), we measure the w_p with two integral constraints for both the best-fitting SHAM catalogues and observations. At first, we use w_p with $\pi_{\max} = 80 h^{-1} \text{ Mpc}$ to obtain a good SNR and avoid the noise-dominated large scales (Mohammad et al. 2020). This π_{\max} value is a common choice for HOD studies (e.g., Avila et al. 2020b). In this case, the w_p of the SHAM for LOWZ samples agrees with the observed w_p , while for CMASS and eBOSS samples, the w_p of SHAM catalogues are generally underestimated compared to those of the observations. We then reduce π_{\max} to $30 h^{-1} \text{ Mpc}$, and the w_p measured from the SHAM and observational catalogues become consistent, as shown in Figures 10–12. Note that π_{\max} values are for both observational and SHAM w_p .

Potential uncorrected systematics that affect the 2PCF monopole on $r \geq 80 h^{-1} \text{ Mpc}$ can explain the inconsistency in w_p with $\pi_{\max} = 80 h^{-1} \text{ Mpc}$. The discrepancy on the large scales of the 2PCF monopole is observed when comparing observations with the galaxy mocks like PATCHY (Kitaura et al. 2016) and EZMOCK (Zhao et al. 2021a). Meanwhile, Huterer et al. (2013) explain that uncorrected photometric systematics can significantly bias clustering on large scales.

To directly demonstrate the consequences of uncorrected systematics on w_p with different π_{\max} , we compare the 2PCF multipoles and projected 2PCFs of EZMOCK mocks without and with observational systematics, respectively. EZMOCK mocks with observational systematics are mocks that mimic the data, including all the systematics mentioned in Section 2.1.3. We do not apply weight corrections, to investigate the potential biases due to systematics. The clustering difference is normalized by the quadrature sum of the standard deviations for EZMOCK mocks with and

¹⁰ <https://www.legacysurvey.org/dr9/files>

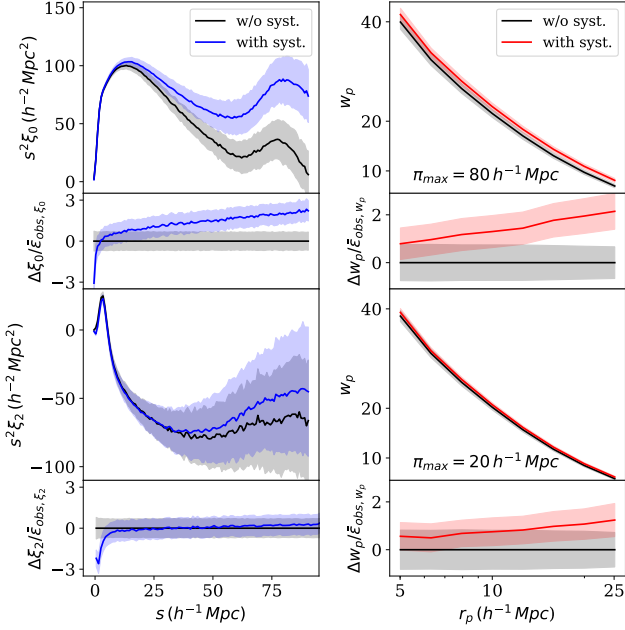


Figure 13. The effect of a biased 2PCF monopole on w_p . The first column represents the 2PCF multipoles of EZMOCK mocks without systematics (black lines with shades) and EZMOCK mocks with systematics (blue lines with shades). The second column is the w_p comparison between EZMOCK mocks without systematics (black lines with shades) and EZMOCK mocks with systematics (red lines with shades). The first row is w_p with π integrating to $80 h^{-1} \text{Mpc}$ and the third row is π integrating to $20 h^{-1} \text{Mpc}$. The second and fourth row for both columns are the difference between their clustering sum by the quadrature sum of the standard deviations for EZMOCK mocks with and without systematics. The w_p difference is suppressed when π_{max} equals a smaller value.

without systematics. As is shown in Fig. 13, the observational systematics is responsible for the monopole difference, especially at scales larger than $50 h^{-1} \text{Mpc}$. Consequently, the bias presented in w_p with $\pi_{\text{max}} = 80 h^{-1} \text{Mpc}$ is much larger than that of w_p with $\pi_{\text{max}} = 20 h^{-1} \text{Mpc}$. The result reveals the importance of properly choosing π_{max} to avoid large-scale systematics as much as possible.

5 CONCLUSION

Subhalo Abundance matching is a powerful method of constructing galaxy catalogue based on high-resolution simulations. We propose a 3-parameter SHAM algorithm that is more general for different galaxy surveys. Besides the classical σ , we introduce v_{smear} that smears the peculiar velocities of SHAM galaxies to model the effect of the redshift uncertainties, and V_{ceil} that removes the most massive haloes/galaxies to account for the completeness of tracers in the massive end due to the target selection (e.g. luminosity threshold).

We construct SHAM catalogues that reproduce the clustering of BOSS/eBOSS LRGs on $[5, 25] h^{-1} \text{Mpc}$ at $0.2 < z < 1.0$, based on the UNIT simulations. The 2PCF multipoles and projected 2PCFs of the SHAM catalogues are consistent with those of BOSS/eBOSS samples, including the entire LOWZ, CMASS and eBOSS samples, and 9 subsamples in different redshift slices. These results validate our new SHAM model. However, for some of the samples such as CMASS at $0.43 < z < 0.7$ and eBOSS LRG $0.7 < z < 0.9$, the best-fitting reduced χ^2 values for the

2PCF multipoles can be larger than 2. This may be due to unknown observational systematics. For the bulk CMASS samples, the inhomogeneity in completeness at different redshift bins can also contribute to the disagreement.

Since the galaxies at $z < 0.6$ are supposed to be complete (Reid et al. 2016), a SHAM model without V_{ceil} should also work for them. This is confirmed by the fitting results except for the CMASS sample at $0.51 < z < 0.57$, which is rejected at more than 4σ . Therefore, the BOSS LRGs should have already been incomplete from $z \approx 0.5$. This finding is especially important for the reconstruction of the stellar mass function.

Using our SHAM method, the 2PCF bias brought by redshift uncertainties can be quantified through the v_{smear} parameter. Meanwhile, we estimate the redshift uncertainty statistically with the redshift difference Δv obtained from repeat observations. There are two estimators of the statistical redshift uncertainties: (1) the best-fitting Gaussian dispersions $\sigma_{\Delta v}$ for the histogram of Δv ; (2) the standard deviations of Δv as $\hat{\sigma}_{\Delta v}$. As expected, both of them increase monotonically with the effective redshift due to broader absorption lines at higher redshifts. Both $\sigma_{\Delta v}$ and $\hat{\sigma}_{\Delta v}$ agree with our CMASS v_{smear} measurements. For eBOSS samples, v_{smear} agrees with the $\hat{\sigma}_{\Delta v}$ measurements while it is in tension with $\sigma_{\Delta v}$. This can be explained by the larger outlier fraction of eBOSS histograms. In short, the standard deviations of the redshift differences are in agreement with v_{smear} for both the CMASS and eBOSS LRG samples.

However, for the BOSS LOWZ sample, there are significant disagreements between v_{smear} values and the redshift uncertainties measured from repetitively observed targets. We have looked into some potential sources of systematic biases including the robustness of subhaloes from the UNIT simulations, the SDSS-III spectroscopic pipeline upgrade and the representativeness of the repeat samples. But none of them can lead to the observed discrepancy. Despite the fact that we have similar satellite fraction for LOWZ and CMASS, it is still possible that LOWZ sample is composed of a different subclass of LRGs that has different satellite properties compared to LRGs from CMASS and eBOSS. To validate this, we need a more detailed SHAM model for LOWZ samples. We leave relevant studies to a future work.

We observe the redshift evolution of eBOSS $\sigma - V_{\text{ceil}}$ posteriors, indicating the sample is more complete at higher redshift bins. With the photometric redshift from DECaLS, we confirm the target selection criteria with a minimum i-band magnitude cut leads to the completeness evolution. Since the scatter parameter σ in our study include both the intrinsic scatter σ_{int} and the incompleteness of galaxy samples, our 2-parameter SHAM measurements provide the constraints on σ_{int} as $\sigma_{\text{int}} < 0.31$ for LOWZ at $0.2 < z < 0.33$, $\sigma_{\text{int}} < 0.36$ for LOWZ at $0.33 < z < 0.43$, and $\sigma_{\text{int}} < 0.46$ for CMASS at $0.43 < z < 0.51$.

The projected 2PCFs of the best-fitting SHAM catalogues are consistent with those of the observations when the integral limit π_{max} is as small as $30 h^{-1} \text{Mpc}$. However, w_p of SHAM catalogues deviates from the observations when $\pi_{\text{max}} = 80 h^{-1} \text{Mpc}$. This can be explained by potential uncorrected systematics that mainly affect large scales. A test based on EZMOCK mocks with and without systematics also proves that w_p evaluated with a π_{max} of around $30 h^{-1} \text{Mpc}$ is less sensitive to systematic effects, compared to w_p with $\pi_{\text{max}} = 80 h^{-1} \text{Mpc}$. The result also supports the choice of a smaller π_{max} when using w_p for SHAM and HOD studies (e.g., Alam et al. 2020).

To conclude, our 3-parameter SHAM model works well for

LRGs at a wide range of redshift, though there are a few exceptions that may be due to uncorrected observational systematics. Our algorithm is also effective in estimating uncertainties of redshift measurements, and detection of sample incompleteness for most of the SDSS samples. We are going to further improve the SHAM model by accounting for more properties, such as the satellite fraction. In the meantime, we also plan to extend our studies to ELGs. Because their star-forming processes are quenched in massive haloes (Kauffmann et al. 2004; Dekel & Birnboim 2006), the parameter V_{ceil} is foreseen to be crucial. Later, we shall also construct multi-tracer SHAM models for different types of tracers with both auto- and cross-correlations for cosmological analysis.

DATA AVAILABILITY

The LOWZ and CMASS clustering and random catalogues, PATCHY mocks are all from SDSS data release 12. For eBOSS, the PIP+ANG weighted clusterings can be provided by FM. The corresponding EZMOC mock can be obtained with request to CZ. The SPALL catalogue used for the redshift difference measurements are publicly available and the code of the redshift uncertainty measurement can be obtained upon the request to JB.

ACKNOWLEDGEMENT

JY, CZ and GF acknowledge support from the SNF 200020_175751 ‘‘Cosmology with 3D Maps of the Universe’’ research grant. GR acknowledges support from the National Research Foundation of Korea (NRF) through Grant No. 2020R1A2C1005655 funded by the Korean Ministry of Education, Science and Technology (MoEST).

Funding for the Sloan Digital Sky Survey IV has been provided by the Alfred P. Sloan Foundation, the U.S. Department of Energy Office of Science, and the Participating Institutions. SDSS-IV acknowledges support and resources from the Center for High-Performance Computing at the University of Utah. The SDSS web site is www.sdss.org.

SDSS-IV is managed by the Astrophysical Research Consortium for the Participating Institutions of the SDSS Collaboration including the Brazilian Participation Group, the Carnegie Institution for Science, Carnegie Mellon University, the Chilean Participation Group, the French Participation Group, Harvard-Smithsonian Center for Astrophysics, Instituto de Astrofísica de Canarias, The Johns Hopkins University, Kavli Institute for the Physics and Mathematics of the Universe (IPMU) / University of Tokyo, the Korean Participation Group, Lawrence Berkeley National Laboratory, Leibniz Institut für Astrophysik Potsdam (AIP), Max-Planck-Institut für Astronomie (MPIA Heidelberg), Max-Planck-Institut für Astrophysik (MPA Garching), Max-Planck-Institut für Extraterrestrische Physik (MPE), National Astronomical Observatories of China, New Mexico State University, New York University, University of Notre Dame, Observatório Nacional / MCTI, The Ohio State University, Pennsylvania State University, Shanghai Astronomical Observatory, United Kingdom Participation Group, Universidad Nacional Autónoma de México, University of Arizona, University of Colorado Boulder, University of Oxford, University of Portsmouth, University of Utah, University of Virginia, University of Washington, University of Wisconsin, Vanderbilt University, and Yale University.

REFERENCES

- Ahumada R., et al., 2020, *ApJS*, 249, 3
 Aihara H., et al., 2011, *ApJS*, 193, 29
 Alam S., et al., 2015, *ApJS*, 219, 12
 Alam S., Ata M., et al. 2017, *MNRAS*, 470, 2617
 Alam S., Peacock J. A., Kraljic K., Ross A. J., Comparat J., 2020, *MNRAS*, 497, 581
 Alam S., Aubert M., et al. 2021a, *Phys. Rev. D*, 103, 083533
 Alam S., et al., 2021b, *Phys. Rev. D*, 103, 083533
 Alam S., et al., 2021c, *MNRAS*, 504, 4667
 Angulo R. E., Pontzen A., 2016, *MNRAS*, 462, L1
 Aubert M., et al., 2020, arXiv e-prints, p. arXiv:2007.09013
 Avila S., et al., 2020a, *MNRAS*, 499, 5486
 Avila S., et al., 2020b, *MNRAS*, 499, 5486
 Bautista J. E., et al., 2021, *MNRAS*, 500, 736
 Behroozi P. S., Conroy C., Wechsler R. H., 2010, *ApJ*, 717, 379
 Bianchi D., Percival W. J., 2017, *MNRAS*, 472, 1106
 Blanton M. R., et al., 2017, *AJ*, 154, 28
 Bolton A. S., et al., 2012, *AJ*, 144, 144
 Bond J. R., Kofman L., Pogosyan D., 1996, *Nature*, 380, 603
 Buchner J., et al., 2014, *A&A*, 564, A125
 Campbell D., van den Bosch F. C., Padmanabhan N., Mao Y.-Y., Zentner A. R., Lange J. U., Jiang F., Villarreal A., 2018, *MNRAS*, 477, 359
 Chaves-Montero J., Angulo R. E., Schaye J., Schaller M., Crain R. A., Furlong M., Theuns T., 2016, *MNRAS*, 460, 3100
 Chuang C.-H., Kitaura F. S., Prada F., Zhao C., Yepes G., 2015, *MNRAS*, 446, 2621
 Chuang C.-H., et al., 2019, *MNRAS*, 487, 48
 Conroy C., Wechsler R. H., Kravtsov A. V., 2006, *ApJ*, 647, 201
 Contreras S., Angulo R. E., Zennaro M., 2021, *MNRAS*, 508, 175
 Dawson K. S., et al., 2012, *AJ*, 145, 10
 Dawson K. S., et al., 2016, *AJ*, 151, 44
 de Mattia A., et al., 2021, *MNRAS*, 501, 5616
 Dekel A., Birnboim Y., 2006, *MNRAS*, 368, 2
 DESI Collaboration et al., 2016, The DESI Experiment Part I: Science, Targeting, and Survey Design (arXiv:1611.00036)
 Dey A., et al., 2019, *AJ*, 157, 168
 du Mas des Bourboux H., et al., 2020, *ApJ*, 901, 153
 Eisenstein D. J., et al., 2011, *AJ*, 142, 72
 Favole G., et al., 2016a, *MNRAS*, 461, 3421
 Favole G., McBride C. K., Eisenstein D. J., Prada F., Swanson M. E., Chuang C.-H., Schneider D. P., 2016b, *MNRAS*, 462, 2218
 Feldman H. A., Kaiser N., Peacock J. A., 1994, *ApJ*, 426, 23
 Feroz F., Hobson M. P., 2008, *MNRAS*, 384, 449
 Feroz F., Hobson M. P., Bridges M., 2009, *MNRAS*, 398, 1601
 Feroz F., Hobson M. P., Cameron E., Pettitt A. N., 2019, *OJAp*, 2, 10
 Gil-Marín H., et al., 2020, *MNRAS*, 498, 2492
 Granett B. R., Favole G., Montero-Dorta A. D., Branchini E., Guzzo L., de la Torre S., 2019, *MNRAS*, 489, 653
 Gunn J. E., et al., 2006, *AJ*, 131, 2332
 Guo Q., White S., Li C., Boylan-Kolchin M., 2010, *MNRAS*, 404, 1111
 Guo H., Zehavi I., Zheng Z., 2012, *ApJ*, 756, 127
 Guo H., et al., 2015, *MNRAS*, 446, 578
 Hartlap J., Simon P., Schneider P., 2007, *A&A*, 464, 399
 Hou J., et al., 2021, *MNRAS*, 500, 1201
 Huterer D., Cunha C. E., Fang W., 2013, *MNRAS*, 432, 2945
 Kaiser N., 1987, *MNRAS*, 227, 1
 Kauffmann G., White S. D. M., Heckman T. M., Ménard B., Brinchmann J., Charlot S., Tremonti C., Brinkmann J., 2004, *MNRAS*, 353, 713
 Kitaura F.-S., Yepes G., Prada F., 2014, *MNRAS: Letters*, 439, L21
 Kitaura F.-S., et al., 2016, *MNRAS*, 456, 4156
 Klypin A., Yepes G., Gottlöber S., Prada F., Heß S., 2016, *MNRAS*, 457, 4340
 Kraljic K., Arnouts S., et al. 2018, *MNRAS*, 474, 547
 Kravtsov A. V., Berlind A. A., Wechsler R. H., Klypin A. A., Gottlöber S., Allgood B., Primack J. R., 2004, *ApJ*, 609, 35
 Landy S. D., Szalay A. S., 1993, *ApJ*, 412, 64

- Lange J. U., Hearin A. P., Leauthaud A., van den Bosch F. C., Guo H., DeRose J., 2022, *MNRAS*, 509, 1779
- Leauthaud A., et al., 2016, *MNRAS*, 457, 4021
- Lewis A., 2019, arXiv e-prints, p. arXiv:1910.13970
- Lin S., et al., 2020, *MNRAS*, 498, 5251
- Lyke B. W., et al., 2020, *ApJS*, 250, 8
- Madau P., Pozzetti L., Dickinson M., 1998, *ApJ*, 498, 106
- Malavasi N., Arnouts S., et al. 2016, *MNRAS*, 465, 3817
- Mohammad F. G., et al., 2020, *MNRAS*, 498, 128–143
- Nagai D., Kravtsov A. V., 2005, *ApJ*, 618, 557
- Neveux R., et al., 2020, *MNRAS*, 499, 210
- Parejko J. K., et al., 2013, *MNRAS*, 429, 98
- Peebles P. J. E., Hauser M. G., 1974, *ApJS*, 28, 19
- Percival W. J., Bianchi D., 2017, *MNRAS*, 472, L40
- Planck Collaboration et al., 2020, *A&A*, 641, A6
- Prakash A., et al., 2016, *ApJS*, 224, 34
- Press W. H., Schechter P., 1974, *ApJ*, 187, 425
- Raichoor A., de Mattia A., et al. 2020, *MNRAS*, 500, 3254
- Reid B. A., Seo H.-J., Leauthaud A., Tinker J. L., White M., 2014, *MNRAS*, 444, 476
- Reid B., et al., 2016, *MNRAS*, 455, 1553
- Rodríguez-Torres S. A., et al., 2016, *MNRAS*, 460, 1173
- Ross A. J., et al., 2014, *MNRAS*, 437, 1109
- Ross A. J., et al., 2016, *MNRAS*, 464, 1168
- Ross A. J., et al., 2020, *MNRAS*, 498, 2354
- Rossi G., et al., 2021, *MNRAS*, 505, 377
- Shan H., et al., 2017, *ApJ*, 840, 104
- Sinha M., Garrison L., 2019, in Majumdar A., Arora R., eds, *Software Challenges to Exascale Computing*. Springer Singapore, Singapore, pp 3–20
- Sinha M., Garrison L. H., 2020, *MNRAS*, 491, 3022
- Smee S. A., et al., 2013, *AJ*, 146, 32
- Smith A., et al., 2020, *MNRAS*, 499, 269
- Steinmetz M., Navarro J., 1999, *ApJ*, 513, 555
- Tamone A., et al., 2020, *MNRAS*, 499, 5527
- Tasitsiomi A., Kravtsov A. V., Wechsler R. H., Primack J. R., 2004, *ApJ*, 614, 533
- Trujillo-Gomez S., Klypin A., Primack J., Romanowsky A. J., 2011, *ApJ*, 742
- Vale A., Ostriker J. P., 2004, *MNRAS*, 353, 189
- Wang Y., Chuang C.-H., Hirata C. M., 2013, *MNRAS*, 430, 2446
- Wang Y., et al., 2020, *MNRAS*, 498, 3470
- Wechsler R. H., Tinker J. L., 2018, *ARA&A*, 56, 435
- White S. D. M., Rees M. J., 1978, *MNRAS*, 183, 341
- Willick J. A., Courteau S., Faber S. M., Burstein D., Dekel A., Strauss M. A., 1997, *ApJS*, 109, 333
- York D. G., et al., 2000, *AJ*, 120, 1579
- Zel'Dovich Y. B., 1970, *A&A*, 500, 13
- Zhai Z., et al., 2017, *ApJ*, 848, 76
- Zhao C., et al., 2021a, *MNRAS*, 503, 1149
- Zhao G.-B., et al., 2021b, *MNRAS*, 504, 33
- Zhao C., et al., 2022, *MNRAS*, 511, 5492
- Zhou R., et al., 2020, *MNRAS*, 501, 3309

APPENDIX A: THE EFFECT OF FIBRE COLLISION

To avoid potential biases of the clustering measurements due to uncorrected fibre collision effects with nearest-neighbour close-pair weights (w_{CP}), we conduct a new SHAM fitting on the monopole and quadrupole in $[10, 25] h^{-1} \text{Mpc}$, which are not significantly affected by fibre collision effects (Guo et al. 2012; Rodríguez-Torres et al. 2016), for LOWZ at $0.2 < z < 0.43$. The resulting posterior distributions of parameters are shown in Fig. A1. As demonstrated in the figure, the constraints are consistent with those from our fiducial fitting range $[5, 25] h^{-1} \text{Mpc}$ at 1σ level. It thus suggests that our SHAM fitting results are robust.

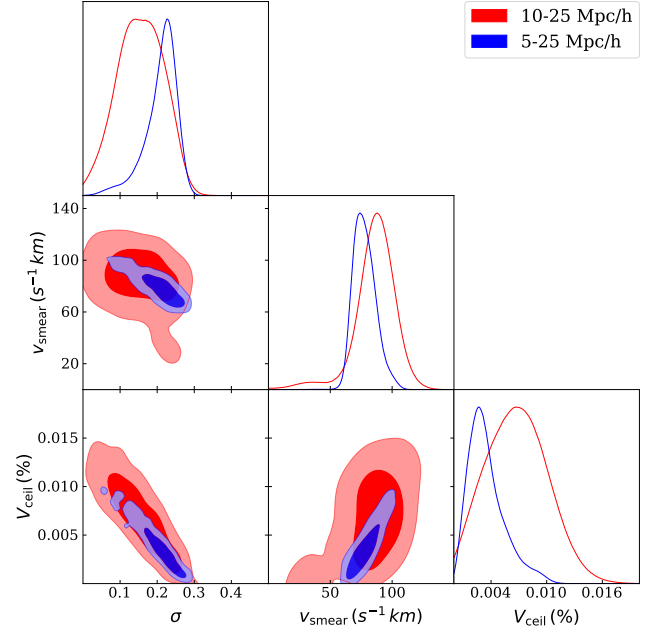


Figure A1. The posteriors of SHAM parameters for LOWZ at $0.2 < z < 0.43$, obtained with the fitting of monopole and quadrupole at ranges on $[10, 25] h^{-1} \text{Mpc}$ (red) and $[5, 25] h^{-1} \text{Mpc}$ (blue).

APPENDIX B: BLUE SAMPLES IN LOWZ

In order to indirectly prove the representative of the repeat observation, we choose to study the fraction of blue galaxies, i.e., f_{blue} in the repeat measurement catalogue and the galaxy clustering catalogue. The differentiation of the blue and red samples is achieved by applying an *ad hoc* criterion on the colour–redshift diagram. For example, with a constant colour cut $(g - i) = 2.35$, Favole et al. (2016b) selects the blue tail of CMASS samples and find out that they have different clustering properties from the red samples. The magnitudes for colour calculation are the Composite Model Magnitudes (i.e., CMODEL MAG; Reid et al. 2016) from the SPALL catalogue. We start with using the same cut on both clustering catalogue and repeated samples for LOWZ and CMASS (Fig. B1 and Fig. B2). The results in Table B1 shows that f_{blue} in clustering samples are quite close to f_{blue} of the repeat samples. Despite of the minor difference, for LOWZ, f_{blue} of the clustering catalogue is always larger than f_{blue} of the repeated samples, while for CMASS it is the opposite. Additionally, there is no significant difference in the $\hat{\sigma}_{\Delta v}$ of blue galaxies and red galaxies that can lead to the disagreement between LOWZ v_{smeat} and LOWZ Δv .

As shown in Fig. B2, a constant cut cannot help to select the blue tail of LOWZ. A cut varies with the redshift is a better choice. So we apply $(g - i) = 2.8z + 1.2$, and find f_{blue} drops to the same level as CMASS with a constant cut. The clustering catalogue still has f_{blue} larger than that of the repeat observations and we have small difference between the red and blue $\hat{\sigma}_{\Delta v}$, just like our findings in the results of the constant cut. The results can be found in Table B2. So it proves that the redshift uncertainties measured based on repeat samples should be representative for the clustering sample.

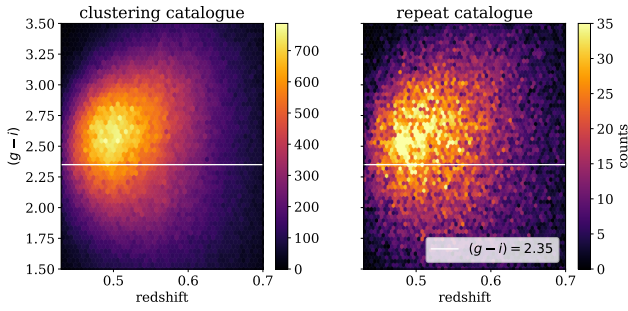


Figure B1. The colour–redshift diagram for CMASS at $0.43 < z < 0.7$ and the blue galaxy threshold (white dashed lines). *Left:* the colour distribution of galaxies from the clustering catalogue. *Right:* the colour distribution of galaxies from the repeat observation.

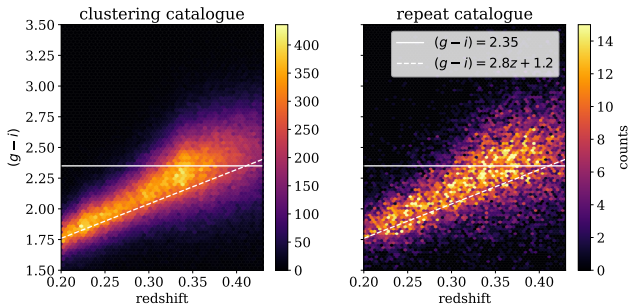


Figure B2. The same as Fig. B1 for LOWZ with two cuts. The first cut is $(g - i) = 2.35$ (the white solid line) and the second one is $(g - i) = 2.8z + 1.2$ (the white dashed line).

APPENDIX C: POSTERIOR OF BOSS AND EBOSS SHAM

The posteriors of all the 3-parameter SHAM results are presented in Figures C1–C6. The top panel of each column shows the marginalized posterior of the parameter written at the bottom. The remaining three panels are the 2D posterior contours. Parameters with the maximum likelihood determined by `PYMULTINEST`¹¹ (Buchner et al. 2014) are marked in the figures. All the posteriors are from converged Monte-Carlo chains of `MULTINEST`. The multi-modal 1D posteriors of σ and V_{ceil} may be due to the noisy data.

We also present the posteriors of the 2-parameter SHAM without V_{ceil} in Figures C7–C9, comparing with those of the corresponding 3-parameter SHAM. We keep the posteriors of V_{ceil} for the convenience of visualizing the $V_{\text{ceil}}-v_{\text{smear}}$ degeneracy.

This paper has been typeset from a $\text{\TeX}/\text{\LaTeX}$ file prepared by the author.

z range	f_{blue} clst. (%)	f_{blue} repeat (%)	red $\hat{\sigma}_{\Delta v}$ ($\text{s}^{-1} \text{ km}$)	blue $\hat{\sigma}_{\Delta v}$ ($\text{s}^{-1} \text{ km}$)
$0.2 < z < 0.33$	88.9	87.3	29.3 ± 3.4	26.0 ± 2.5
$0.33 < z < 0.43$	46.1	44.6	33.1 ± 1.7	33.1 ± 3.6
$0.2 < z < 0.43$	67.3	64.6	32.5 ± 1.5	28.8 ± 2.2
$0.43 < z < 0.51$	37.3	37.5	46 ± 2.7	48.3 ± 4.7
$0.51 < z < 0.57$	36.3	37.4	52.8 ± 3.4	52.6 ± 3.0
$0.57 < z < 0.7$	37.0	38.8	61.0 ± 3.6	60.7 ± 4.8
$0.43 < z < 0.7$	36.9	38.0	54.0 ± 1.9	54.6 ± 2.8

Table B1. The f_{blue} for the clustering catalogue and the repeat observation, and the $\hat{\sigma}_{\Delta v}$ of the blue and the red galaxies for LOWZ and CMASS samples at different redshift bins using the constant cut $(g - i) = 2.35$. The f_{blue} values of LOWZ clustering catalogue are larger than those of the repeat catalogue, while CMASS samples shows the opposite relation. The difference between the red and blue $\hat{\sigma}_{\Delta v}$ is not significant for LOWZ and CMASS.

z range	f_{blue} clst. (%)	f_{blue} repeat (%)	red $\hat{\sigma}_{\Delta v}$ ($\text{s}^{-1} \text{ km}$)	blue $\hat{\sigma}_{\Delta v}$ ($\text{s}^{-1} \text{ km}$)
$0.2 < z < 0.33$	30.9	29.1	26.8 ± 2.9	25.7 ± 1.7
$0.33 < z < 0.43$	30.5	30.2	32.7 ± 1.4	34.1 ± 5.1
$0.2 < z < 0.43$	30.7	29.7	30.0 ± 1.5	30.5 ± 3.2

Table B2. The same as Table B1 for LOWZ using the redshift cut $(g - i) = 2.8z + 1.2$. The f_{blue} s of clustering are still larger than those of the repeat catalogue and the difference between the red and blue $\hat{\sigma}_{\Delta v}$ is also small.

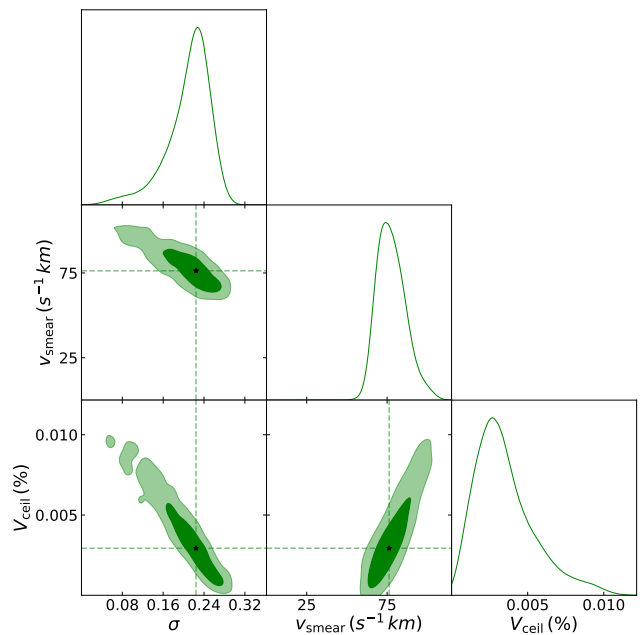


Figure C1. The posteriors of SHAM parameters for LOWZ samples at $0.2 < z < 0.43$. The black dots in the contours indicate the position of the best-fitting parameters.

¹¹ <https://github.com/JohannesBuchner/PyMultiNest>

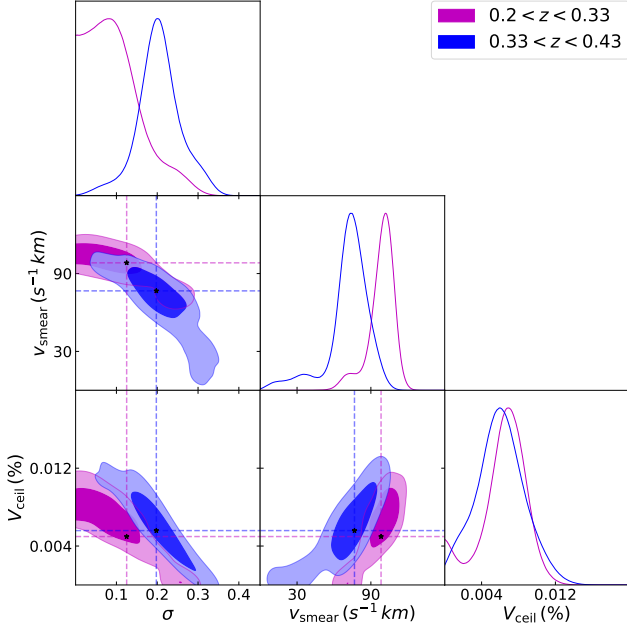


Figure C2. The same as Fig. C1 for LOWZ SHAM at $0.2 < z < 0.33$ (magenta) and $0.33 < z < 0.43$ (blue).

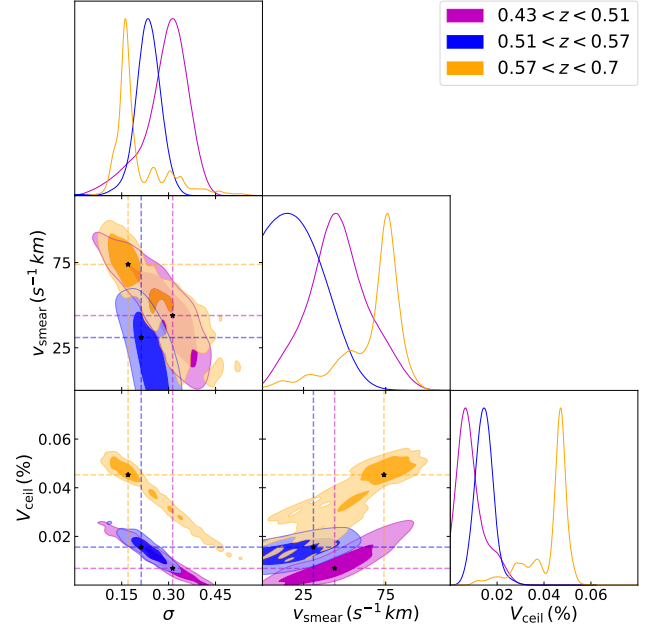


Figure C4. The same as Fig. C1 for LOWZ SHAM at $0.43 < z < 0.51$ (magenta), $0.51 < z < 0.57$ (blue) and $0.57 < z < 0.7$ (orange).

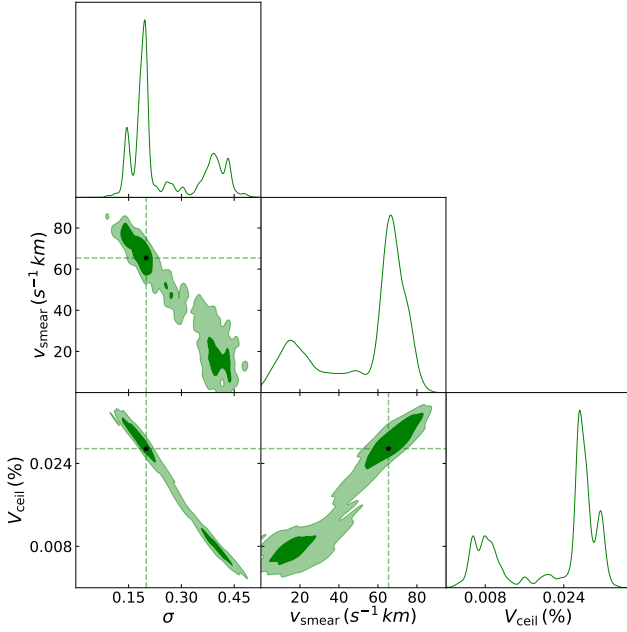


Figure C3. The same as Fig. C1 for CMASS SHAM at $0.43 < z < 0.7$.

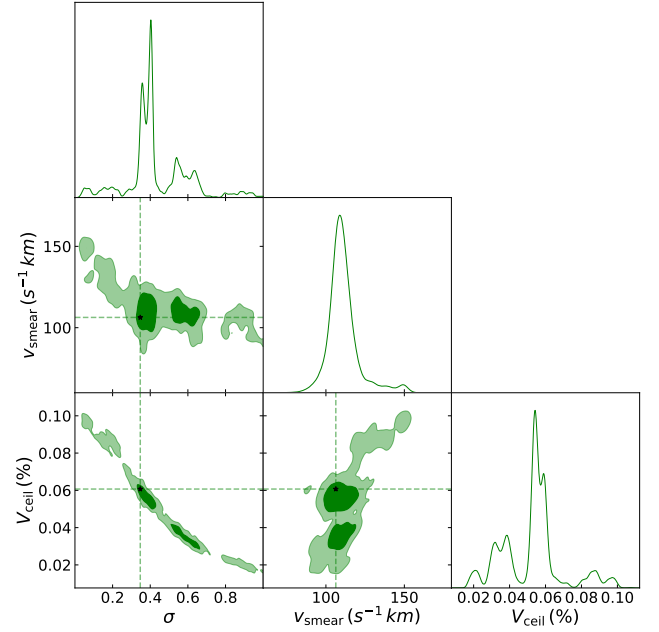


Figure C5. The same as Fig. C1 for eBOSS LRG SHAM at $0.6 < z < 1.0$.

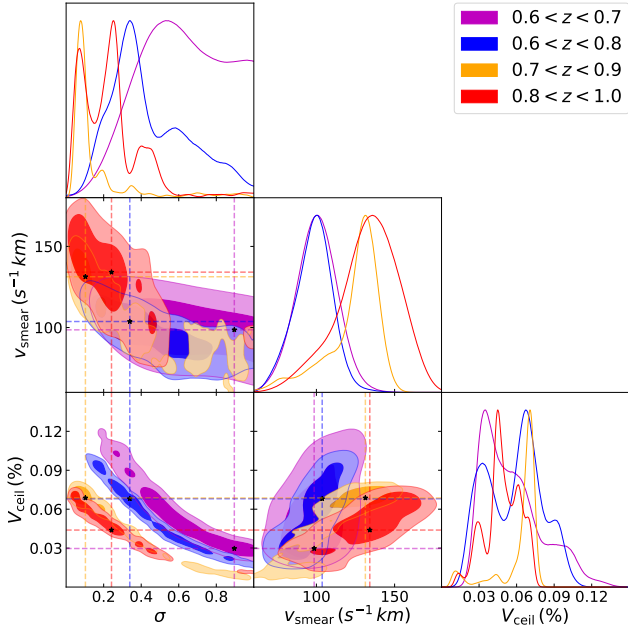


Figure C6. The same as Fig. C1 for eBOSS LRG SHAM at $0.6 < z < 0.7$ (magenta), $0.6 < z < 0.8$ (blue), $0.7 < z < 0.9$ (orange) and $0.8 < z < 1.0$ (red). The evolution of the σ - V_{cell} contour indicates the incompleteness at higher redshift bins is lower than that of the lower redshift bins as explain in Section 4.3.

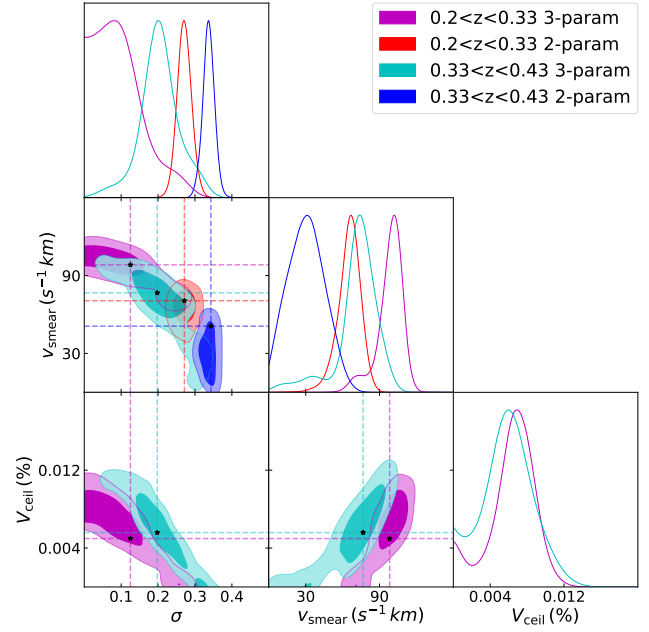


Figure C8. The same as Fig. C7 for LOWZ SHAM comparisons at $0.2 < z < 0.33$ (magenta, red) and $0.33 < z < 0.43$ (cyan, blue).

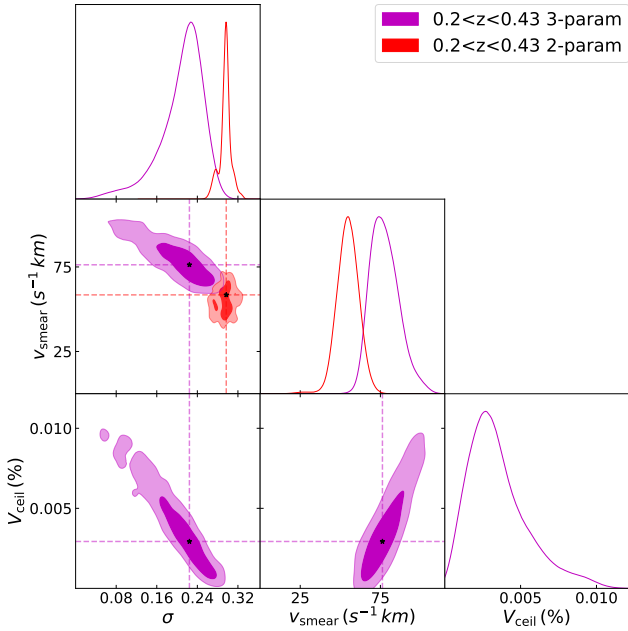


Figure C7. The posteriors of 3-parameter SHAM (magenta) compared with 2-parameter SHAM (red) for LOWZ samples at $0.2 < z < 0.43$.

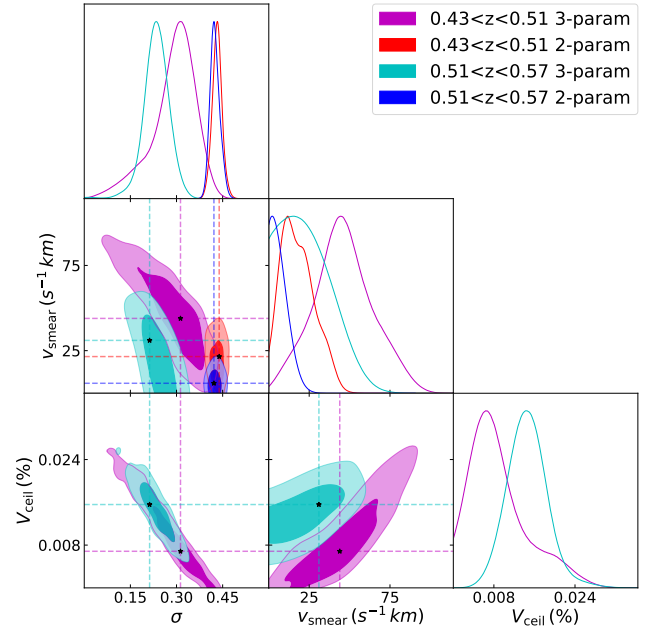


Figure C9. The same as Fig. C7 for CMASS SHAM comparisons at $0.43 < z < 0.51$ (magenta, red) and $0.51 < z < 0.57$ (cyan, blue).